Turun yliopisto
University of Turku

DEVELOPMENT OF 3D SUPER-RESOLUTION TOMOGRAPHIC STED MICROSCOPY AND ITS APPLICATION TO STUDIES ON BONE RESORPTION

Takahiro Deguchi

TURUN YLIOPISTON JULKAISUJA – ANNALES UNIVERSITATIS TURKUENSIS
Sarja - ser. D osa - tom. 1208 | Medica - Odontologica | Turku 2015

University of Turku

Faculty of Medicine
Institute of Biomedicine
Department of Cell Biology and Anatomy
University of Turku Doctoral Programme of Molecular Medicine (TuDMM)
Medicity Research Laboratories
Laboratory of Biophysics

Supervised by

Professor Pekka Hänninen, Ph.D.
Laboratory of Biophysics
Department of Cell Biology and Anatomy
University of Turku
Turku, Finland

Tuomas Näreoja, Ph.D.
Department of Neuroscience
Karolinska Institutet
Stockholm, Sweden

Reviewed by

Professor John Eriksson, Ph.D.
Cell Biology Department of Biosciences
Abo Akademi University
Turku, Finland

Professor Thomas Klar, Ph.D.
Institute of Applied Physics
Johannes Kepler University
Linz, Austria

Opponent

Teng-Leong Chew, Ph.D.
Advanced Imaging Center
Howard Hughes Medical Institute
Janelia Research Campus
Ashburn, Virginia, USA

ISBN 978-951-29-6316-4 (PRINT)
ISBN 978-951-29-6317-1 (PDF)
ISSN 0355-9483
Painosalama Oy - Turku, Finland 2015

To my family, my friends,
and my mentor

Takahiro Deguchi

Development of 3D super-resolution tomographic STED microscopy and its application to studies on bone resorption

Faculty of Medicine, Institute of Biomedicine, Department of Cell Biology and Anatomy, University of Turku Doctoral Programme of Molecular Medicine (TuDMM), Medicity Research Laboratories, Laboratory of Biophysics, Turku, Finland

Annales Universitatis Turkuensis, Medica-Odontologica Painosalama, Turku 2015

Abstract

In this doctoral thesis, a tomographic STED microscopy technique for 3D super-resolution imaging was developed and utilized to observe bone remodeling processes. To improve upon existing methods, we have used a tomographic approach using a commercially available stimulated emission depletion (STED) microscope. A certain region of interest (ROI) was observed at two oblique angles: one at a standard inverted configuration from below (*bottom view*) and another from the side (*side view*) via a micro-mirror positioned close to the ROI. The two viewing angles were reconstructed into a final tomogram. The technique, named as tomographic STED microscopy, was able to achieve an axial resolution of approximately 70 nm on microtubule structures in a fixed biological specimen.

High resolution imaging of osteoclasts (OCs) that are actively resorbing bone was achieved by creating an optically transparent coating on a microscope coverglass that imitates a fractured bone surface. 2D super-resolution STED microscopy on the bone layer showed approximately 60 nm of lateral resolution on a resorption associated organelle allowing these structures to be imaged with super-resolution microscopy for the first time.

The developed tomographic STED microscopy technique was further applied to study resorption mechanisms of OCs cultured on the bone coating. The technique revealed actin cytoskeleton with specific structures, comet-tails, some of which were facing upwards and some others were facing downwards. This, in our opinion, indicated that during bone resorption, an involvement of the actin cytoskeleton in vesicular exocytosis and endocytosis is present.

The application of tomographic STED microscopy in bone biology

demonstrated that 3D super-resolution techniques can provide new insights into biological 3D nano-structures that are beyond the diffraction-limit when the optical constraints of super-resolution imaging are carefully taken into account.

Keyword: Stimulated emission depletion (STED) microscopy, tomographic microscopy, axial super-resolution, osteoclast, bone resorption

Takahiro Deguchi

Tomografisen STED super-resoluutio mikroskooppitekniikan kehittäminen, sekä sen sovellus luu biologian tutkimuksessa

Solubiologia ja anatomia, Biofysiikan laboratorio, Biolääketieteen laitos, Lääketieteellinen tiedekunta, molekyylilääketieteen tohtoriohjelma (TuDMM), Turun Yliopisto, Turku

Lääketieteenllinen tiedekunta, Biolääketieteen laitos, Solubiologia ja anatomia, Turun Yliopisto molekyylilääketieteen tohtoriohjelma (TuDMM), Biofysiikan laboratorio, Turku, Suomi

Annales Universitatis Turkuensis, Medica-Odontologica Painosalama, Turku 2015

Tiivistelmä

Väitöskirja käsittelee STED super-resoluutio kerroskuvausmikroskooppitekniikan kehittämistä, sekä sen sovellusta luuston uusiutumisprosessin havainnoinnissa. Tekniikka kehitettiin kaupallista STED mikroskooppia hyödyntäen. Kerroskuvausmenetelmä perustuu näytteen kuvaamiseen kahdesta eri suunnasta, alta sekä sivusta; sivunäkymä muodostettiin mikroskooppinäytteen päälle, kuvattavan kohteen yläpuolelle vinosti asetetun pienen peilin kautta, jonka jälkeen projektiot yhdistetään laskennallisesti yhdeksi kerroskuvaksi. STED kerroskuvaustekniikka mahdollisti solun sisäisten mikroputkirakenteiden havainnoinnin 70nm pitkittäisresoluutiolla.

Pystyäksemme kuvaamaan luuta aktiivisesti resorpoivia osteoklastisoluja korkealla optisella erottelukyvyllä, kehitimme mikroskooppilasille muodostettavan, optisesti läpinäkyvän pinnoitteen, joka imitoi murtunutta luupintaa. Pinnoite mahdollisti osteoklastisolujen luun resorptioon liittyvien soluelinten kuvantamisen 2D STED mikroskooppia käyttäen 60 nm lateraaliresoluutiolla; tämä on ensimmäinen kerta kun kyseisiä solurakenteita on pystytty kuvaamaan super-resoluutio mikroskoopilla.

Käytimme kehitettyä tomografista STED tekniikkaa osteoklastisolujen resorptiomekanismin kuvantamisessa, uutta läpinäkyvää luupinnoitetta hyväksikäyttäen. Tomografiatekniikalla muodostetuista kuvista voidaan nähdä aktiini tukirakenteiden spesifisiä rakenteita, jotka meidän mielestämme viittaavat niiden osallistumiseen vesikkeleiden endo- ja eksosytoosiin luun resorptioprosessin aikana.

Tomografinen STED mikroskopia, yhdistettynä uuteen luupinnoitteeseen avaa uusia mahdollisuuksia kolmiulotteisten nanorakenteiden havainnointiin, tutkittaessa luuston uusiutumisprosessia.

Avainsanat: STED mikroskopia, tomografinen mikroskopia, pitkittäis super-resoluutio, osteoklastit, luun resorptio

CONTENTS

ABBREVIATIONS

2D	Two dimensional
3D	Three dimensional
AP	Actin patch
APD	Avalanche photo diode
BSA	Bovine serum albumin
CME	Clathrin-mediated endocytosis
FSD	Functional secretory domain
FWHM	Full width at half maximum
GSD	Ground state depletion
GSDIM	Ground state depletion followed by individual molecule return
iPALM	Interferometric photoactivated localization microscopy
NA	Numerical aperture
OC	Osteoclast
PALM	Photoactivated localization microscopy
PD	Podosome
PEM	Patterned excitation microscopy
PFA	Paraformaldehyde
PSF	Point spread function
RB	Ruffled border
RESOLFT	Reversible saturable optical fluorescence transitions
ROI	Region of interest
RP	Resorption pit

SAR	Small actin ring
SIM	Structured illumination microscopy
SNR	Signal-to-noise ratio
SSIM	Saturated structured illumination microscopy
STED	Stimulated emission depletion
STORM	Stochastic optical reconstruction microscopy
SZ	Sealing zone
TDE	2,2′-thiodiethanol
TIRF	Total internal reflection
uPAINT	Universal point accumulation for imaging in nanoscale topography

LIST OF ORIGINAL PUBLICATIONS

This thesis is based on the following original publications, which are referred to by their Roman numerals I – III in the text. In addition, some unpublished results are included in the thesis.

I. Takahiro Deguchi, Sami Koho, Tuomas Näreoja, and Pekka Hänninen. "Axial Super-Resolution by Mirror-Reflected Stimulated Emission Depletion Microscopy." Optical Review 21, no. 3 (May 1, 2014): 389–94.

II. Takahiro Deguchi, Maria, Alanne, Elnaz, Fazeli, Katja, M. Fagerlund, Paula, Pennanen, Petri, Lehenkari, Pekka, E. Hänninen, Juha, Peltonen, and Tuomas, Näreoja. 2014. "In Vitro Model of Bone to Facilitate Measurement of Adhesion Forces and Super-Resolution Imaging of Osteoclasts." Submitted manuscript.

III. Takahiro Deguchi, Sami V. Koho, Tuomas Näreoja, Juha Peltonen and Pekka Hänninen. "Tomographic STED microscopy to study bone resorption" Proceedings of SPIE, T. G. Brown, C. J. Cogswell, and T. Wilson, eds. (2015), p.93301M.

1 INTRODUCTION

Far-field optical microscopy is a favored tool to study many biological and medical research problems because, unlike near-field or electron microscopy techniques, it provides a flexible applicability in applications aimed at revealing details and processes in a realistic environment. The resolution of any imaging system is defined as an ability to distinguish two separate objects within a small distance. In far-field light microscopy, the optical resolution is limited, due to the diffraction of light, and was described by well-known definitions; the Abbe criterion and Rayleigh criterion (Abbe, 1873; Rayleigh, 1903). According to the criteria, the *diffraction-limited* optical resolution is about a half of the wavelength used, and even with modern optical systems, e.g. confocal microscopy with high numerical aperture objective lens, any two objects closer than about 200 nm could not be seen separately in diffraction-limited far-field optical microscopy.

Recently developed techniques, super-resolution microscopy or optical nanoscopy, provide resolution far beyond the diffraction-limited resolution in fluorescence microscopy. In these techniques, the diffraction of light is no longer the primary determinant of resolution. The first demonstrated technique among all the super-resolution microscopy techniques is stimulated emission depletion (STED) microscopy. In this study, the improvement of resolution in three dimensional (3D) STED microscopy, providing diffraction-unlimited resolution is discussed. Any other improvement is distinguished as "resolution enhancement." This study focuses especially on the resolution improvement in the axial direction (z-direction) along the optical axis of the microscope system and this is in contrast to the lateral direction (x-y direction), which is perpendicular to the optical axis. Optical systems providing super-resolution in lateral and axial directions are referred to as *3D super-resolution microscopy*. Different approaches for achieving 3D super-resolution are also reviewed here.

In addition, applications of the 3D super-resolution techniques in solving biological questions are discussed and a study on bone biology is presented. The osteoclast (OC) is a unique cell with its abilities of multi-nuclei cell formation and bone resorption, and it has gained scientific interest due to its relation and importance in bone diseases. Within osteoclast biology, studies focusing on the role that the actin

cytoskeleton plays during bone resorption are discussed. In this study, for further understanding of actin cytoskeleton function during OC resorption, an application of 3D super-resolution STED microscopy together with a newly developed OC culture method is described. Lastly, the experimental validation and an indication of the role that actin plays in bone resorption are discussed.

2 REVIEW OF THE LITERATURE

In the following chapters super-resolution microscopy is introduced with an insight into studies of bone biology. The first section of the review focuses on the super-resolution techniques. Firstly, two dimensional (2D) optical super-resolution microscopy is introduced. Secondly, improvements of the axial resolution in super-resolution techniques for 3D optical super-resolution microscopy are described.

The second section describes methodologies of osteoclast (OC) optical investigations concerning the actin cytoskeleton in relation to bone resorption. Firstly, the basic biology of OC and the importance of the actin cytoskeleton during bone resorption are introduced. Secondly, osteoclast culture substrates for optical microscopy are described. Thirdly, optical investigations into the actin cytoskeleton in OC are discussed.

2.1 Far-field optical super-resolution microscopy

The available resolution of an optical microscope was limited because of the diffraction of light until the end of the 20th century. This limitation was overcome when the first super-resolution techniques, namely stimulated emission depletion (STED) (Hell and Wichmann, 1994) and ground state depletion (GSD) (Hell and Kroug, 1995), were introduced. Over the last decade, the refinement and introduction of different super-resolution modalities has completely changed our understanding of resolution capabilities of optical microscopes, and currently, they provide resolution down to a few nanometers (Wildanger et al., 2012). The resolution improvement has been expanded to all three dimensions, and the techniques have been applied to study 3D structures of biological specimen to provide valuable new biological insights (Schmidt et al., 2009; Shtengel et al., 2009).

2.1.1 Optical resolution in the light microscope

Ernst Abbe was the first to derive a concise mathematical presentation of the optical resolution and proposed that the best resolution of any

optical system with a circular aperture is described by the formula,

$$d = \frac{\lambda}{2NA} \tag{1}$$

where d is the optical resolution or minimal distance between two objects to be separated, λ is the wavelength, and NA is the numerical aperture of the objective lens specifying the focusing angle of the optics and the refractive index. This limit of possible best resolution in an optical system has been considered an unbreakable barrier in light microscopy for more than 100 years (Abbe, 1873). In widefield optical microscopy, the resolution is explained by light diffracted at two point objects. At least the first order diffraction maxima needs to be collected to resolve the two objects, so a higher numerical aperture (NA) objective lens is needed to achieve a higher resolution. This is practically limited due to space constraint up to about pi collection angle or NA of 1.45 with an oil immersion objective lens. In laser scanning confocal microscopy, optical resolution can be described as the focal volume or the product of illumination and detection spots or point spread functions (PSF). Optical resolution increase is approached by different methods in reducing the extent of these PSFs. The main determinant of the size of diffraction PSF is again the numerical aperture of an objective lens used. Here, approaches to change the shape of PSF are discussed.

Later, a ring-shape aperture or annular pupil for resolution improvement in an optical system was proposed (di Francia, 1952). The concept of annular aperture was experimentally demonstrated through microscopy (Sheppard, 1977), and the same group achieved a full width at half maximum (FWHM) of focal spot less than 100 nm in solid immersion setup with annular pupil aperture together with radial polarization (Sheppard and Choudhury, 2004). However, as di Francia explained in his work, the approach is very limited in the detection of light, because most of the light is blocked, limiting practical application. Further, the inherent property of this technique in suppressing the low frequency (low detail) components within the aperture is that all high frequency components are amplified yielding a PSF with several side maxima laterally and a severe extension of the PSF (worsening of resolution) in axial direction due to poor axial confinement of the wavefront.

However, in the axial direction, there have been several successful ideas to overcome the NA limit of a single objective lens by coherent use of two light paths. The resolution improvements were achieved by 4pi microscopy and its widefield counterpart implementation, I^5M (Gustafsson et al., 1995), in which light at focus from two objective lenses were coherent to produce interference. Standing wave microscopy (Bailey et al., 1993) utilizes similar approach but with standing wave excitation illumination. These techniques have improved axial resolution, down to 100 nm or even better. However, the enhanced resolution achieved by these techniques was based on a coherent use of light from the objective lenses, e.g., interference of light at an optical focus, axially reducing the focal volume, so that the diffraction nature of the light still limited the resolution in the techniques. Moreover, the coherent use did not affect the PSF in lateral direction, so it provided a focal volume reduction, but the lateral resolution remained the same.

2.1.2 Super-resolution microscopy

In mid 1990s, two groups suggested that the diffraction barrier can theoretically be circumvented in far-field fluorescence light microscopy. Hell et al. claimed this by reducing effective PSF in confocal microscopy by utilizing stimulated emission (Hell and Wichmann, 1994) or triplet states of fluorescent molecules (Hell and Kroug, 1995) and Betzig by localizing positions of individual emitters sequentially (Betzig, 1995). The former two concepts were experimentally demonstrated; STED microscopy in 1999 and 2000 (Klar and Hell, 1999; Klar et al., 2000), and GSD microscopy in 2007 (Bretschneider et al., 2007). The latter concept lead to the discovery and demonstration of photoactivated localization microscopy (PALM) utilizing a photoactivatable fluorescent protein (Patterson and Lippincott-Schwartz, 2002) in 2006 (Betzig et al., 2006). These techniques were realized based on the same principle; *photoswitching* fluorescent molecules between two distinct states; *dark* and *bright* or *on* and *off* states. The molecules are switched on and off within a diffraction-limited distance to be differentiated. The mechanism of the photoswitching for resolution improvement is well described in (Hell, 2004) and is shown in Figure 1.

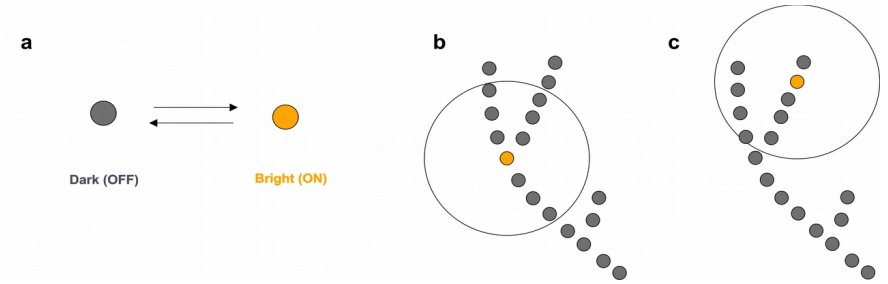

Figure 1: Photoswitching concept (modified from Hell, 2004). Molecular states, dark and bright (a), are controlled within diffraction-limit (b and c) such that only single or a few emitters emit so their positions are known or solved from recorded images. The circles represent the areas of the diffraction-limited resolution.

Stimulated Emission Depletion (STED) microscopy and the generalized concept of RESOLFT

In STED microscopy, fluorophores in the diffraction-limited focal spot undergo two types of emission: spontaneous emission at the center and controlled (and saturated) stimulated emission at the outer regions of the focal spot. The mechanisms of the two types of emissions are described in the Figure 2.

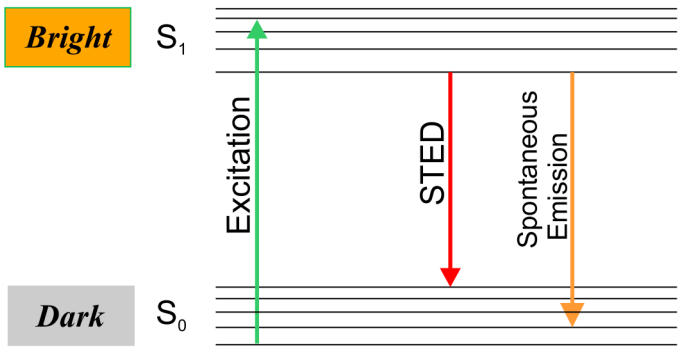

Figure 2: Jablonski diagram for STED (Adapted from Hell, 2003). Molecules excited to S_1 (Bright) state are "switched off" by STED beam to S_0 state (Dark) under the STED beam and emit longer wavelength photons than spontaneous emission photons.

STED microscopy utilizes two laser beams in confocal microscopy: the excitation beam and high intensity spatially modified beam, called STED beam. The two beams are overlapped on top of each other. Fluorescent molecules illuminated by the excitation beam are excited to the first singlet state. After vibrational relaxation, the excited molecules are illuminated with the STED beam and "switched off" through stimulated emission to the ground state (Figure 2). The photons from stimulated emission are at the same wavelength, phase, polarization and direction as the STED beam. The wavelength of the STED beam is set to overlap the tail of the emission spectrum, such that the photons have a longer wavelength compared with the majority of spontaneous emission photons and therefore can be filtered out. By overlaying a doughnut shape STED beam on the excitation beam, molecules at the doughnut center are allowed spontaneous emission, while others under the STED beam are switched off and do not emit spontaneous photons. As shown in Figure 3 this results in a reduction in the effective excitation volume, and thus the resolution improves (Hell, 2009). Using the non-linear nature of saturation of the depletion, the theoretical STED resolution is not diffraction-limited. This stimulated emission can be exaggerated by increasing the intensity of the STED beam and at least in the theoretical formula, STED microscopy approaches infinite resolution. The resolution of STED microscopy is practically limited with dye bleaching (destruction) and optical aberrations setting the true resolution limit. The resolution in STED microscopy can be described with the following equation (Willig et al., 2006);

$$d_{sted} = \frac{\lambda}{2NA\sqrt{(1+I/I_{sat})}} \tag{2}$$

where d_{sted} is the resolution in STED microscopy, I is the intensity of STED beam at the focal spot, and I_{sat} is the *saturation threshold intensity* at which most of the fluorophores undergo stimulated emission.

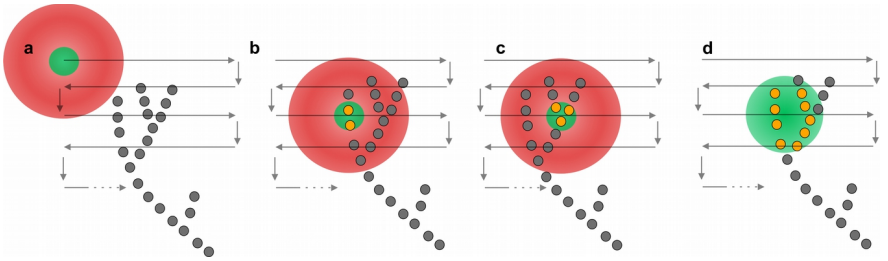

Figure 3 STED microscopy (Adapted from Hell, 2009). (a) A sample is scanned with overlapping excitation (green) and STED (red) beams. (b) In STED microscopy, molecules under STED beam are switched off (gray), and only those at the center are allowed spontaneous emission (orange). Thus a less number of molecules are recorded from each pixel, and (c) molecules within the diffraction-limited area can be still distinguished as it scans. (d) In confocal microscopy, the excitation spot is diffraction-limited, so a larger number of molecules is excited simultaneously.

The STED effect on microscopic scale was spectroscopically presented (Hell, Schrader, et al., 1995) demonstrating quenching spontaneous emission by STED beam. Later STED microscopy succeeded to show an approx. 30 % improvement (Klar and Hell, 1999). In the latter work, authors overlapped two Gaussian shape beams with a slight offset. This caused a STED effect only in a part of the excitation spot resulting in PSF reduction and resolution improvement. Later STED microscopy with a doughnut shaped depletion beam was demonstrated (Klar et al., 2000). The STED beam effectively switched off the excited fluorophores at the outer part of the excitation beam, providing better reduction in the effective PSF volume. STED was also later demonstrated with continuous excitation and depletion lasers (Willig et al., 2006) and later on with pulsed excitation and continuous depletion lasers with time-gated detection (Vicidomini et al., 2011). STED has been widely applied in biological and live animal samples (Berning et al., 2012; Bethge et al., 2013; Klar et al., 2000; Nägerl et al., 2008; Schneider et al., 2015; Urban et al., 2011), demonstrating a wide applicability of the technique in biological studies.

STED microscopy utilizes a concept known as reversible saturable optical fluorescence transitions (RESOLFT). In microscopy techniques based on RESOLFT, two distinct states (dark and bright) and non-linearity of fluorescent molecules are controlled within a diffraction-limited area. The concept was described well in (Hell, 2003, 2004), but

already utilized in earlier works (Hell and Kroug, 1995; Hell and Wichmann, 1994). In addition to STED and GSD microscopy, RESOLFT microscopy with switchable fluorescent proteins or switchable organic dyes has been proposed based on RESOLFT concept. As dark and bright states GSD utilizes first excited and triplet states, and RESOLFT microscopy utilizes fluorescent and non-fluorescent states of photoswitchable molecules. Both have been demonstrated experimentally in biological samples (Bretschneider et al., 2007; Hofmann et al., 2005), and later RESOLFT microscopy proved its good applicability in live samples due to its low illumination intensity and fast imaging capability (Chmyrov et al., 2013).

Localization microscopy

In localization microscopy, the on and off states are controlled stochastically. PALM was the first demonstrated localization microscopy technique and it worked in a widefield fluorescence microscopy scheme using a concept of single molecule switching (Dickson et al., 1997). In order to avoid multiple fluorescent molecules within the diffraction-limited area, which emit photons simultaneously such that they diffract and overlap with each other on the detector, a single molecule within the diffraction-limited distance is switched on, while the others are kept at an off state (Figure 4). A researcher, using PALM and all stochastic techniques, can record the positions of these two molecules separately, by statistically switching them on. The on-off switching is achieved from a photoactivation property of specific fluorescent proteins in PALM (Betzig et al., 2006). By illuminating with a low power blue laser, a few fluorescent molecules within illumination area are randomly activated and enabled to luminesce. Once activation is complete, the activated molecules are luminescent under the excitation light while the other non-activated molecules remain dark. Thus only the emitting (activated) molecules contribute to the camera image. Once an image is acquired, the centroids of the molecules are precisely localized from the acquired image and each location is recorded on a virtual (or reconstructed) image. After the localization, the molecule is switched off by photobleaching. The cycle is repeated until positions of all molecules within the field of view have been recorded (Figure 4).

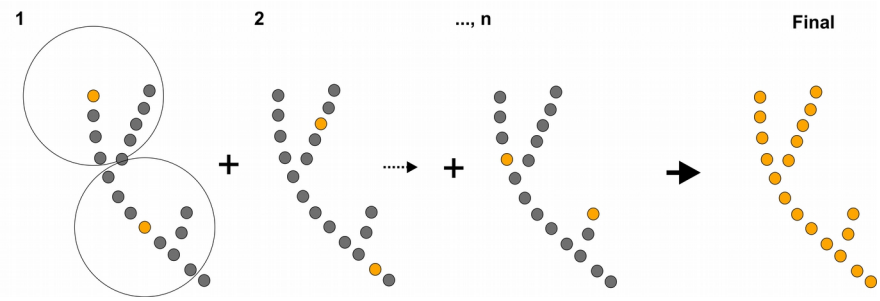

Figure 4 Localization microscopy (Adapted from Hell, 2009). (1) Only a single molecule within diffraction-limited distance (black circle) is activated to bright state (orange) and localized, while the other molecules are kept in dark state (gray). (2) In the next image, another different set of molecules are activated and localized. This is repeated n times, and a final image is reconstructed with all the localized molecules.

The precision of the centroid localization determines the resolution of localization techniques, and in a simple case in which shot noise is dominant, it is described with an equation (Thompson et al., 2002):

$$\Delta x = \frac{s}{\sqrt{m}} \tag{3}$$

where s is the standard deviation of the PSF, and m is the number of detected photons from each activated fluorophore before it bleaches. It is worth noting that m varies from one molecule to another, therefore the localization precision also varies. To ensure a certain localization precision, molecular events with a low number of photon emission are often discarded. Localization microscopy has achieved a resolution close to 20 nm in a focal plane (Bates et al., 2007). The average number of emitted photons is, in practice, limited due to photobleaching, such that the attainable resolution in localization is limited in most cases.

Since the first publication of PALM, a variety of localization techniques has been introduced. The next technique after PALM was stochastic optical reconstruction microscopy (STORM) (Rust et al., 2006). In STORM, the on and off states were controlled by photoswitching of fluorophores. Unlike photoactivation in PALM, in

STORM molecular states go from dark to bright and then go back to dark state after spontaneous emissions. However, besides the switching mechanism, the technical principles are nearly identical. Later, the localization technique was realized with normal organic dyes, e.g., Alexa Fluor, etc. The technique called “direct STORM (dSTORM)” utilizes, similarly to GSD, the triplet state of fluorophores. By taking advantage of the triplet state, which has a longer lifetime, the technique achieves the dark state enabling on-off switching (Heilemann et al., 2008). dSTORM is often referred also as GSDIM, which stands for Ground State Depletion followed by Individual Molecule Return (Fölling et al., 2008). To avoid the usual bleaching of triplet populated molecules dSTORM/GSDIM is performed with a specific mounting media (van de Linde et al., 2011; Olivier et al., 2013). In another localization technique, Universal Point Accumulation for Imaging in Nanoscale Topography (uPAINT), on-off switching is achieved by random molecular binding onto a cell membrane (Giannone et al., 2010; Sharonov and Hochstrasser, 2006). It utilizes random bindings of diffusing fluorescent molecules in solution and fluorescence emission is detected when the molecules are bound to a sample surface. Since the mounting medium contains nearly an unlimited number of fluorescent molecules, in practice, fluorescence does not deplete completely. The technique, uPAINT, is capable of live imaging with possible lower phototoxicity, but the imaging is limited on membrane surfaces.

Localization microscopy is a simple approach and can be achieved with inexpensive light sources without any scanning elements, but it requires a camera with a fast readout and high sensitivity. On the other hand, it does not provide direct resolution improvement, but effective resolution improvement from stochastic imaging and post computational processes. Because of this feature, localization microscopy has several drawbacks. Firstly, it can create artifacts due to imprecise or inaccurate molecular localizations. Several articles summarized important aspects to be considered in localization microscopy, including sources of artifacts (Deschout et al., 2014; Endesfelder and Heilemann, 2014). Authors stressed the importance of fitting algorithms to be used for precise localization depending on the emitter properties. Secondly, it was pointed out that localization accuracy of fluorescent emitters in 3D sample depends on the orientation of transition dipole and an offset from the focal plane (Engelhardt et al., 2011). Thirdly, in general, localization microscopy requires a longer time for image acquisition. Imaging of podosome

dynamics in live cells with a temporal resolution of 4 seconds was demonstrated using localization microscopy (Cox et al., 2012). However, compared to other super-resolution techniques like STED, the localization technique is not currently favorable in live sample imaging.

Structured illumination microscopy (SIM)

Another approach, called structured illumination microscopy (SIM) or patterned excitation microscopy (PEM), achieved super-resolution in fluorescence microscopy by modulating excitation light into a specific pattern structure. The principle originates in an idea that Moire fringes created by a combination of illumination pattern and sample details appear larger in size compared with the original sample details (Heintzmann and Cremer, 1999). By imaging with the structured illumination, information beyond the diffraction-limited resolution is shifted to within the diffraction-limit in a process called “aliasing” (Shroff et al., 2008), and therefore super-resolution information is gained. However, during the process information at a certain area that is in this so-called k-space is lost. To compensate for the loss of information, a set of images from the same area are acquired with different illumination pattern. For the ease of image acquisition and reconstruction, a striped illumination pattern with different angles is commonly used. After acquiring a series of images, they are transformed to Fourier space and reconstructed in k-space, then inverse-transformed for a reconstruction. Using the SIM technique Gustafsson demonstrated a lateral resolution of 110 nm in biological samples (Gustafsson, 2000). In the improved version of the technique, called saturated SIM (SSIM) that utilizes the non-linearity of fluorescence saturation, the achievable resolution is no longer theoretically limited. However, achieving higher resolution requires a higher illumination intensity and a larger set of images to be acquired, and therefore this causes significant photobleaching in many cases. Gustafsson demonstrated a 50 nm lateral resolution, but only in non-biological samples (Gustafsson, 2005).

SIM is relatively fast in image acquisition when compared to localization techniques and can be implemented in a rather simple microscopic setup. Moreover, it is not limited to any specific dye, so it gives a wide selection in fluorescent labeling. However, SIM is also not pure optical microscopy and requires post image processing

through Fourier transformation, which can create artifacts in typical noisy fluorescence images. Therefore unlike STED microscopy demonstrated deep in tissue (Urban et al., 2011), SIM has not been demonstrated in such scattering sample, but only in highly transparent samples (zebrafish embryo) at the depth of 45 μm (York et al., 2012). Although a theoretical resolution of SSIM is not limited, achievable resolution improvement is two to three times in practice, and this is significantly worse compared to STED or localization microscopy.

2.1.3 3D super-resolution microscopy

In optical microscopy, the axial resolution is generally inferior to the lateral resolution due to elongation in focus along optical axis. In confocal microscopy axial resolution is described, e.g., as follows (Corle and Kino, 1996);

$$z = \frac{0.89\,\lambda}{n - \sqrt{(n^2 - NA^2)}} \tag{4}$$

where z is the axial resolution and n is the refractive index. This is approximately 3 to 5 times worse than the lateral resolution, and in 2D super-resolution techniques the mismatch becomes even greater. Using NA of 1.45 instead of the commonly used NA of 1.4, they achieved an axial FWHM of 330 nm in confocal two-photon excitation microscopy (Blanca and Hell, 2002). However, due to the physical space constraint on practical microscope setup further NA increase is a challenge and further resolution improvement by this approach is limited.

Physical limitations of illumination and detection

One of the simplest methods for axial super-resolution beyond the diffraction-limit is physically limiting illumination and detection in the range of super-resolution by slicing a sample into thin sections. This approach is used widely in electron microscopy. By sectioning a sample into 100 nm thick slices, axial super-resolution imaging was demonstrated (Micheva and Smith, 2007; Nanguneri et al., 2012). All the slices were imaged and later reconstructed into a 3D stack, generating 3D information of an original sample. In this way, the axial

PSF of the system does not matter, because the acquired information comes only from the thin section whose thickness is beyond the diffraction-limit. In the thin-sectioning approach, reconstruction of many thin slices into a single 3D image stack is a challenge because of alignment precision. During the reconstruction, each slice is rotated, tilted, and translated to match adjacent slices using a computer, but there is always a possibility of misalignment. In addition, sections can be damaged during slicing. Therefore, physical modifications of the sample between different z-sections do not guarantee reconstruction of original sample structure and thus can cause artifacts.

PSF reshaping

During the initial stage of localization microscopy, lateral resolution was improved, but not axial resolution. To avoid out-of-focus light in a widefield approach, a total internal reflection fluorescence (TIRF) microscopy scheme was utilized (Betzig et al., 2006; Rust et al., 2006), limiting the illumination and thus emission within the evanescent field above a microscope coverglass. However, TIRF is a near-field approach and imaging depth was practically limited to the bottom of the cell in TIRF setup, which restricts the technique to 2D super-resolution on the surface of the sample holder.

This problem was solved using astigmatism and axial super-resolution was achieved in a localization technique (Huang et al., 2008). For this purpose, a cylindrical lens was inserted at the back aperture of an objective lens introducing astigmatism, such that PSFs from molecules at different axial positions are distorted differently. By differentiating molecular axial positions from the degree of distortion and localizing molecular positions in virtual image, axial resolution was improved. With the technique, authors achieved approximately 100 nm axial resolution. Later, the localization precision was improved by introducing a phase filter instead of a cylindrical lens, achieving approximately 60 nm resolution in biological sample (Lee et al., 2012). The inherent limitation of this approach is that the axial localization is limited within the range of focal volume of the objective lens used, which is typically 500 – 700 nm, and experimental results with larger z-range has not been reported yet.

Modulated light

In the first implementation of STED microscopy, the resolution was improved in all three dimensions, achieving 3D super-resolution (Klar et al., 2000). By introducing a pi shift, the shape of the depletion beam yielded a lateral doughnut shape with "caps" below and above the focal plane along optical axis. However, with this setup, the lateral resolution improvement was not dramatic, and the resolution reached only close to 100 nm. To improve the lateral resolution, later studies split the depletion beam into two paths creating lateral and axial doughnuts (Harke et al., 2008). With the combination of the two depletion beams, authors have achieved dramatic improvements reaching 43 nm lateral and 125 nm axial resolution. However, as mentioned in the equation (2), the achievable spatial resolution in STED microscopy is dependent on the depletion beam intensity in focus. By splitting the depletion beam into two optical paths to create the two different doughnuts, the beam intensity for a single doughnut is decreased and therefore the resulting resolution is compromised (Harke et al., 2008). This can be compensated by increasing the depletion beam power, but higher power in focus could cause damage to the samples and, in practice, can limit the achievable resolution. Moreover, it is reported that based on computational simulations axial doughnut is more prone to local change of refractive index in a sample compared to lateral doughnut (Mark et al., 2015). Therefore, higher resolution degradation of axial resolution is expected with axial doughnut in a complex or thick sample.

Gustafsson et al. have demonstrated 3D super-resolution in SIM scheme, where modulated illumination light created a 3D lattice-like pattern (Gustafsson et al., 2008). The 3D-SIM has the same challenges as the 2D SIM: acquiring higher harmonic information is limited by the significant photobleaching and computational post-processing may introduce artifacts in noisy images. To our knowledge, the best experimentally shown axial resolution is 250 nm (Schermelleh et al., 2010), which is worse than STED or localization techniques.

Two opposing objective lenses

In early 1990s, 4pi microscopy improved axial resolution in confocal microscopy using two opposing objective lenses (Hell and Stelzer, 1992). Together with two-photon excitation, it decreased the size of PSF in the axial direction down to 100 nm (Hänninen et al., 1995).

This brought the axial resolution to similar or even better than lateral resolution. A similar approach in widefield microscopy was demonstrated using standing wave excitation (Bailey et al., 1993) and in I^5M (Gustafsson et al., 1999, 1995). Even the resolution improvement was only in the axial direction in these techniques, they were combined with 2D super-resolution techniques to provide super-resolution in three dimensions.

STED microscopy was implemented in 4pi microscopy scheme to improve axial resolution, called 4pi-STED (Dyba and Hell, 2002), demonstrating 33 nm axial FWHM. The STED beam was modified through a phase plate with pi-shift in the middle of the aperture, creating not only an x-y doughnut, but also a z doughnut. Because both the excitation and detection was done only with one objective lens but depletion was done with two opposing objective lenses, the resolution improvement was fully realized by the STED depletion. Later another technique called isoSTED was published, where lateral and axial depletion beams were utilized in a 4pi depletion-setup (Schmidt et al., 2008). Since the two objective lenses were used for excitation, depletion, and collection of emitted photons, focal volume reduction was significantly improved from the first 4pi-STED publication. The isoSTED demonstrated an isotropic PSF of 40 nm in all directions.

In one of the 3D localization microscopy techniques, called interferometric photoactivable localization microscopy (iPALM), the opposing lens approach has achieved an axial resolution of 15 nm with axial interferometric detection (Shtengel et al., 2009). In this technique, the authors set up three optical detection paths at different phases in order to obtain signal variation depending on an axial position of a fluorophore at photoactivation. From the signal pattern at each three detectors, axial position is determined. This has given the best reported axial resolution in 3D super-resolution fluorescence techniques so far.

3D super-resolution techniques with two objective lenses provide significant resolution improvements, yet they require complex and sensitive systems with interferometric based illumination and detection. Also the techniques are based on interferometry between two optical paths from two separate objective lenses, so any refractive index change on the optical path can distort interference at the detector. This, again, implies a limited use of the techniques in thicker samples.

Multi-angle view reconstruction

Imaging a sample from different angles provides a possible gain in axial resolution. The PSF of a microscope system is elongated along the optical axis, so changing the observation angle changes the sharpness of an image, respectively. The idea is to utilize the superior lateral resolution in the axial direction.

Multi-angle view microscopy has been used to gain in axial resolution. In the technique, information from multiple views is collected and utilized to achieve 3D isotropic resolution. Initial work in this field simply acquired and compared multiple views (Skaer and Whytock, 1975), but later work extracted higher frequency information from each view and combined them into a final 3D image (Shaw et al., 1989), called a "tomogram." This approach, widely used in medical imaging, is called "tomography."

To generate multiple views from a single specimen, the target is often observed either by rotating an optical axis or physically rotating the sample. In order to have another view without sample rotation, a smooth reflective surface has been used as a mirror and the target is viewed via the mirror (Figure 5 a). Several studies have shown that micro-mirrors can be used to generate views at multiple angles (McMahon et al., 2009; Seale et al., 2008). These techniques were used to track dynamic movements of small particles or cells in 3D space, and for that particular purpose, images needed to be acquired with a low numerical aperture objective lens with a large field of view and subsequent poor depth discrimination imposed by the low NA. A similar approach with a NA 1.3 objective lens in widefield microscopy was demonstrated revealing chromatin dynamics in yeasts at improved 3D resolution, yet the technique was still diffraction-limited and did not provide super-resolution (Hajjoul et al., 2009). In the examples, reconstruction was done by calculating the molecular coordinates from the mirror angle and optical path length (Berglund et al., 2009, 2010).

The first demonstration of axial super-resolution with a micro-mirror approach was published by Tang et al. (Tang et al., 2010). In this study, authors set a mirror in their sample and the ROI was imaged from two different angles, using a 60x NA1.2 water immersion objective lens in an inverted microscope. The mirror served in generating a view with an angle of either 45 or 54.7 degrees (side view) in addition to a normal observation angle (bottom view). The system was based on PALM and PAINT super-resolution techniques, and the bottom view

provided super-resolution localization in an x-y plane, whereas the side view through the mirror in a y-z plane. By combining the acquired x-y-z coordinate information of the molecules and assigning them in a virtual 3D image, 3D super-resolution was achieved in the final image. Authors claimed an approximately 20 nm localization precision with a calibration sample and sub-100 nm precision in fixed bacterial and neuronal samples. In the setup, the authors split a field of view into two areas, with one focusing directly to the sample (bottom view) and another via the mirror (side view) with a longer path in the sample. This allowed simultaneous monitoring of ROI from two angles at focus, whereas the setup limited the field of view significantly. The advantage in this technique is that only two views were needed to localize molecular positions in 3D space, therefore unlike other work (McMahon et al., 2009; Seale et al., 2008), the authors used a single surface reflector. Because the original resolution of the system was lateral 2D super-resolution but diffraction-limited in axial direction, unlike other 3D super-resolution techniques with a single view (z-doughnut, isoSTED), image recording along the optical axis does not require higher sampling rate than conventional imaging. Therefore, it preserves fluorescent molecules better from photobleaching.

Multiple view microscopy by physical sample rotation was first demonstrated by Skaer et al. (Skaer and Whytock, 1975). In the work, authors tilted their sample up to 30 degrees in either direction and imaged with 100x NA1.25 oil immersion objective lens in differential interference contrast microscopy. In another work, authors demonstrated a tomographic reconstruction in widefield fluorescence microscopy (Shaw et al., 1989). They acquired z-stack images at up to 45 degrees in each direction by tilting the sample on Drosophila melanogaster embryo using a 63x NA1.2 water immersion objective lens. The authors showed a reconstruction of multiple views, typically at three different angles from widefield 3D z-stacks, resulting in axial resolution enhancement and contrast improvement in the final tomogram. A tilting system capable of sample rotation from 0 up to 180 degrees using a 100x NA1.3 oil immersion objective lens was developed (Bradl et al., 1992) and later the system was further improved for 360 degrees rotation (Bradl et al., 1994). This approach was applied into confocal microscopy with a 3D z-stack approach, which enhanced resolution and contrast in the final tomogram compared to the previous widefield approaches (Bradl et al., 1996; Cogswell et al., 1996).

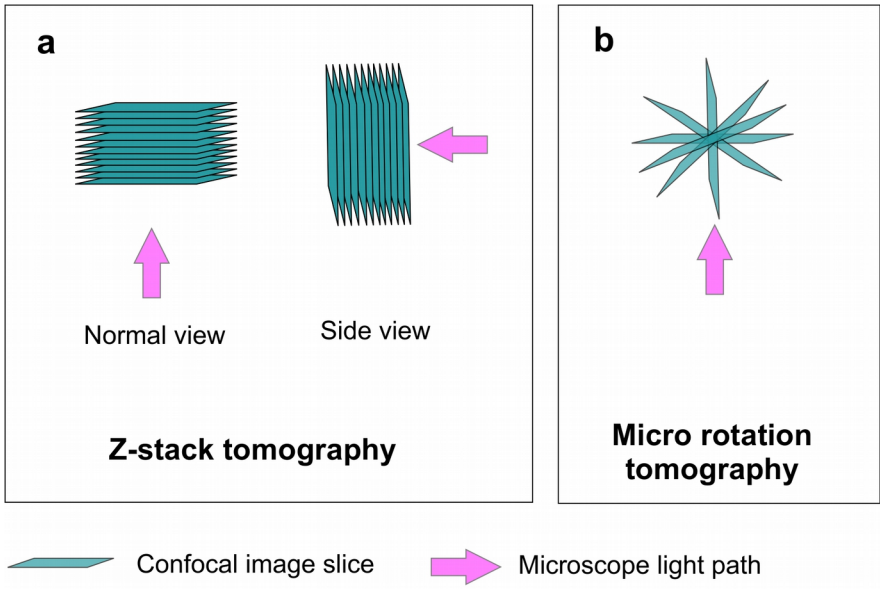

Figure 5: Tomographic microscopy (Modified from Saux et al., 2009 and Laksameethanasan et al., 2006). (a) In 3D z-stack tomography, a 3D z-stack is acquired from several angles. Each z-stack acquires full spatial information of ROI at a given resolution. (b) In micro-rotation tomography, a single slice is acquired at multiple angles. The distance between adjacent slices increases at the edges, therefore, more number of views are required to cover the whole volume of the ROI.

In parallel to the tomographic reconstruction with 3D z-stack approach, micro-rotation imaging was proposed and demonstrated (Lizundia et al., 2005). In the technique one acquires a single image at each angle of rotation (Figure 5 b). As theoretically explained in the work by Laksameethanasan et al., the technique requires typically more than tens of angles to acquire full information of the target, because the outer edges of each view has longer distances to the adjacent views (Laksameethanasan et al., 2006). It was pointed out that, when the rotation center is away from the geometrical center of the target, the risk of missing information is increased (Saux et al., 2009). This means that more views are needed in case of an inaccurate rotation. In 3D z-stack tomography, each observation can scan an entire area of sample (Figure 5 a). Therefore, the 3D z-stack approach is superior to the micro-rotation approach in reducing the number of

views.

In tomographic microscopy, acquired images at multiple angles are combined into one final 3D tomogram. Combining multiple views is essential to utilize all the gained high frequency information in the final tomogram. This process requires two steps; image *registration* in which multiple views are precisely aligned in 3D space, and image *fusion* in which multiple views are combined into a final image with maximum amount of possible high frequency components included. As it was pointed out that, because of the risk for artifacts and resolution degradation from poor registration of multiple views, especially with a Fourier transformation based algorithm, the image registration needs to be precise in order to gain the best possible resolution enhancement (Sätzler and Eils, 1997). On the other hands, to utilize all the high frequency information in the final tomogram, the fusion algorithm of the multi-view is of high importance as well. For this purpose, computational algorithms for image registration and fusion have been developed. The first implementation of a multiple view reconstruction microscopy was demonstrated by Shaw's group (Shaw et al., 1989). Over the last few years, the improvements in reconstruction algorithms have been reported and software for semi-automated registration and fusion has become widely available (Remmele et al., 2011; Rubio-Guivernau et al., 2012).

The PSF volume reduction with different number of views and different fusion algorithms in confocal 3D z-stack tomography were compared (Sätzler and Eils, 1997). In the work, the authors concluded that by reconstructing a tomogram with eight views, the enhancement of resolution and image contrast was significantly improved compared to two or four views. Later, it was demonstrated that with only three views isotropic PSF can be achieved both in simulation and experiments, thus succeeding in decreasing the number of views by improving reconstruction algorithms (Heintzmann and Cremer, 2002). In their work, they demonstrated resolution enhancement and significant improvements in contrast and an isotropic 3D view in biological samples.

In comparison with the sample rotation approach, the advantage of the multi-view approach with mirrors is that the sample does not have to be rotated and therefore, the sample can be a routinely used microscope coverglass with cultured cells on top. This advantage gives more freedom in sample preparations for wider applications of the technique.

2.2 Optical investigation of osteoclasts and their functions

Osteoclasts (OCs) are in charge of bone resorption and play an essential role in bone remodeling in human metabolism through resorbing damaged bone and releasing resorption products, such as bone minerals like calcium and collagens, to extracellular spaces. In an adult individual, this bone remodeling process is held in balance because bone density remains and possible injuries are "routinely" corrected. When this bone remodeling loses its balance, a risk of bone-related diseases is increased. In its most severe form, excess bone resorption leads to osteoporosis.

Bone resorption processes are not fully understood due to their inherent complexity. It appears that only a true environment stimulates correct OC behavior and this fact makes detailed *in vitro* studies difficult (Destaing et al., 2003; Geblinger et al., 2010; Lakkakorpi et al., 1989). Therefore, creating better functioning tools for studies of osteoclast bone resorption mechanisms and its regularization are of high interest.

In the following, the biology behind OC resorption with an emphasis on the subject of this thesis, creation of better tools for OC resorption studies, is briefly reviewed.

2.2.1 Osteoclast subcellular structures and bone resorption

Bone resorbing OC is a polarized cell with specific subcellular organelles and structures, such as ruffled border (RB), sealing zone (SZ), functional secretory domain (FSD), basolateral membrane (Takahashi et al., 2014; Teitelbaum, 2000). OCs are often found at indentations in the bone surface, called resorption pits (RP) (Figure 6). RB is a complexly folded membrane structure and has been considered as an active resorption organelle (Väänänen and Horton, 1995). OCs resorb bone under acidic environments, and in order to create the low pH area at RB, OCs secrete protons together with resorption associated proteins, such as various matrix metalloproteinases, tartrate-resistant acid phosphatase, and collagenase by exocytosis (Teitelbaum, 2000). During OC bone resorption, SZs surround the acidic environment by

isolating RB from the outer intracellular space (Väänänen and Horton, 1995). Minerals and fragmented collagen, degraded from bone, are endocytosed at RB membranes, and the endosomes are transferred to the secretory domain of the OCs by a vesicular transcytosis mechanism (Stenbeck, 2002). Finally the resorption products are released from the secretory domain of OCs into extracellular space (Nesbitt and Horton, 1997; Salo et al., 1997).

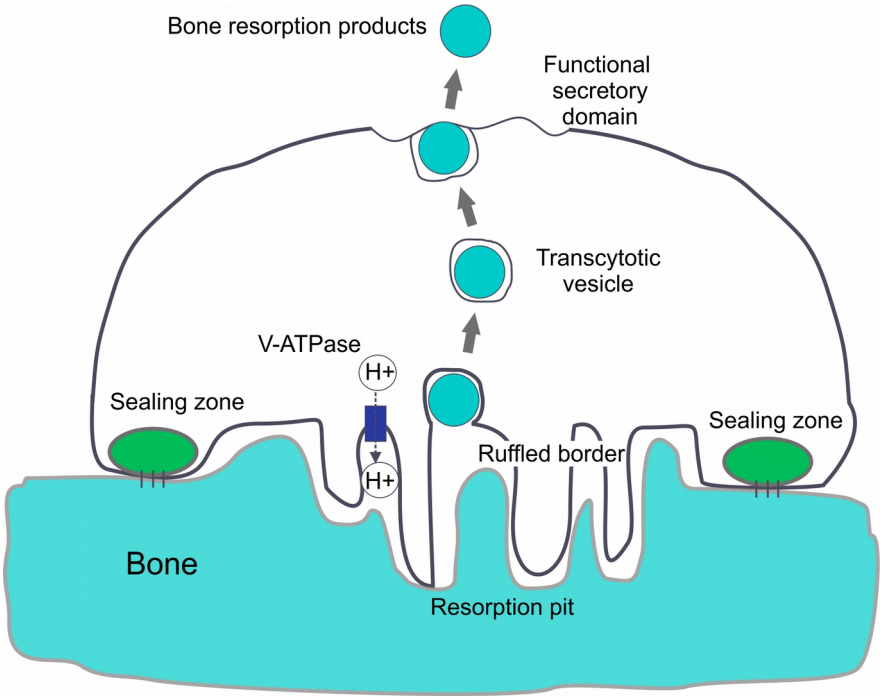

Figure 6: Osteoclast at bone resorption (Simplified from Takahashi et al., 2014). OC is a expressing sealing zone as an adhesion structure, ruffled border as a resorption site, and functional secretory domain. Protons are secreted to the resorption pit, and resorption products are transported to extracellular spaces from functional secretory domain via vesicular transcytosis.

2.2.2 The expected role of actin cytoskeleton in osteoclast bone resorption

The actin cytoskeleton is found in most eukaryotic cells and it plays an essential role in cellular dynamics, e.g., cell motility. Actin filaments (f-actin) are helical polymers with two strands consisted of the protein

actin. F-actin can exist as a single filament, in bundles, or in networks. F-actin has distinct plus and minus ends, and actin monomers bind to the plus end to extend filaments, while the filaments disassemble from the minus end to retract. The polymerization of actin is reversible, and this provides assembly and disassembly of f-actin to generate rapid cytoskeletal rearrangements in cellular dynamics (Dominguez and Holmes, 2011). At leading edges of cells, plasma membranes are often protruded and these dynamic morphological changes are driven by actin extension/polymerization. One of actin-binding proteins, myosin II is known as a motor protein along f-actin to support the protrusion during the cell motility (Vicente-Manzanares et al., 2009).

F-actin can form a variety of structures, such as branches, curved meshes, assembled bundles, loosely-packed or tightly-packed parallel bundles, and the formation of these structures are regulated by a variety of actin-binding proteins, such as the Arp complex, filamin, fimbrin, profilin, and α-actinin (Small et al., 2002). Actin is also known for force generation as it polymerizes and branches (Theriot, 2000), not only in muscles but in other biological functions, and the generated force is expected to be involved in cellular functions, such as exocytosis, endocytosis, podosome (PD) formation, and phagocytosis. During a type of endocytosis event, clathrin-mediated endocytosis (CME), f-actin may play a key role by force generation during membrane invagination, scission of budding endosomal vesicles, and following transportation of the vesicles away from the membrane (Collins et al., 2011; Mooren et al., 2012; Rust and Maritzen, 2015; Smythe and Ayscough, 2006) (Figure 7). During these events, branching of f-actin forms specific bundles with thicker heads called *comet-tail* structures that hold clathrin-coated structures (Cameron et al., 2001; Svitkina, 2013) (Figure 7 b).

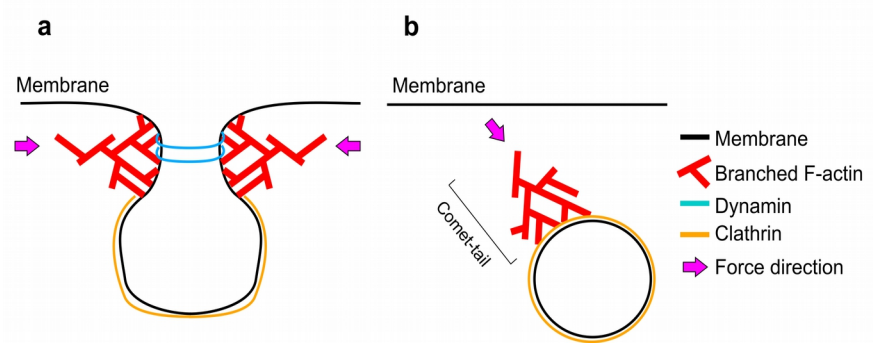

Figure 7: Clathrin-mediated endocytosis (CME) (Simplified from Collins et al., 2011). (a) Clathrin forms an invagination of membrane. Branching f-actin generates force and helps to close the invagination and dynamin completes the vesicle formation with scission. (a, b) The branching f-actin, known as comet-tail, pushes the membrane and vesicles during and after endocytosis.

OC is known for expressing different actin morphologies; a podosome which is a cluster of an actin spot and mostly found on non-bone substrates (Marchisio et al., 1984); sealing zones (SZ) which is a thick f-actin ring; and actin patch (AP) or cloud of f-actin whose function is unknown (Luxenburg et al., 2007; McMichael et al., 2010; Szewczyk et al., 2013).

Podosomes are subcellular structures with dense cores of f-actin surrounded by adaptor proteins and focal adhesion proteins (Figure 8), well described in (van den Dries et al., 2013), and they can be found in OCs but also in other cells, e.g., macrophages or dendritic cells. The adaptor proteins include vinculin, talin, and paxillin, and the focal adhesion proteins include a variety of integrins. These proteins form a ring-shape around the actin cores. PDs are known as adhesion machinery of cells with highly dynamic structures (Destaing et al., 2003; Luxenburg et al., 2012) and form protrusions at plasma membranes in dendritic cells (Gawden-Bone et al., 2010). It was proposed that PDs work as sensors to probe and sense the extracellular environment (van den Dries et al., 2014).

OCs express PDs mainly on non-bone related substrates, such as glass and plastics and they often form a dense ring of PDs called PD belts or PD rings (Pfaff and Jurdic, 2001). Electron micrographs have shown that PDs have interconnecting f-actin networks between individual cores (Luxenburg 2007) and each filament extends in radial fashion

from the core (Akisaka and Yoshida, 2015). PD-like structures are also found on bone-related substrates (Akisaka and Yoshida, 2015). A switch of SZ to PD belts in live OCs on a bone-mimicking substrate was experimentally shown and it was suggested that PDs are organized into SZ (Saltel et al., 2004), however, the direct transformation has not been demonstrated yet. OC bone resorption is reduced when an adhesion protein, αVβ3 integrin, in PDs is inhibited and it is suggested that the integrin-dependent signaling is needed for OC bone resorption (Duong and Rodan, 1999; Novack and Faccio, 2011).

SZ mostly appears as a continuous thick ring of f-actin in fluorescence microscopy with a typical ring width of 5 μm and it is often used as a marker for sites of bone resorption in OCs. In electron microscopy, SZ appears as assemblies of dense actin networks, sometimes with PD-like actin clusters (Akisaka and Yoshida, 2015; Luxenburg et al., 2007). Although, SZ was introduced as an adhesion structure to bone (Väänänen and Horton, 1995) and is widely accepted, the mechanisms of its formation and adhesion at molecular level are not fully known. For example, complete f-actin colocalization with dynamin in confocal images was demonstrated (Bruzzaniti et al., 2005). The suggested role of dynamin is to regulate clathrin-coated pits maturation and vesicle formation during clathrin-mediated endocytosis (CME) (Mettlen et al., 2009), and these have not been explained well in relation with the suggested SZ function.

At RB, active exocytosis and endocytosis are expected to secrete proton pumps such as V-ATPase (Stenbeck, 2002) and bone degrading enzymes and to remove resorption products, respectively (Väänänen and Horton, 1995). Past studies suggested massive vesicular transcytosis at RB (Nesbitt and Horton, 1997; Palokangas et al., 1997; Salo et al., 1997), and recent studies suggested that CME is present (Akisaka and Yoshida, 2015; Akisaka et al., 2006; Mulari et al., 2003).

On the inside of SZ, where RB is expected, f-actin structures, such as APs (McMichael et al., 2010) and clouds (Szewczyk et al., 2013) have been found. A variety of proteins have been localized at such resorption sites, such as integrin B3 (Mulari et al., 2003), V-ATPase (Szewczyk et al., 2013), clathrin (Akisaka and Yoshida, 2015; Akisaka et al., 2006; Mulari et al., 2003), and dynamin (Mulari et al., 2003) as resorption associated proteins, and the Arp complex for branching actin formation (Irene Rita and Maragos Hurst, 2006). Clathrin is a key protein in CME, which forms membrane invaginations for vesicle generations (Kaksonen et al., 2006), and dynamin has been suggested,

in association with membrane invagination and scission (pinching) of the budding vesicles, to complete endocytosis events (Mettlen et al., 2009) (Figure 7). The presence of these proteins with the Arp complex strongly indicates f-actin association with the proteins during CME events at RB, and therefore, visualization of f-actin structures in detail within AP at RB is desired for indications of the involvement of f-actin in the endocytosis mechanism.

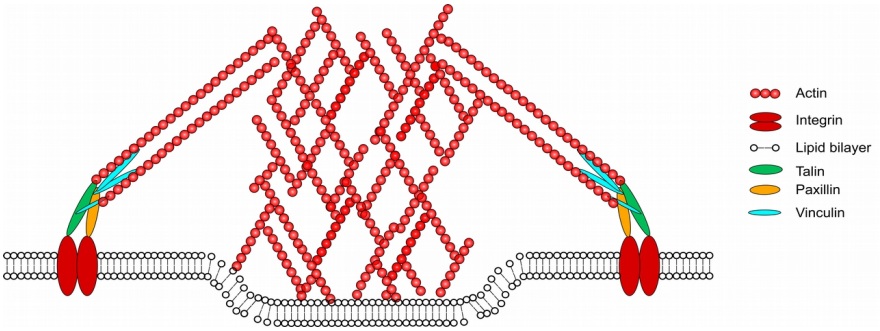

Figure 8: Podosome structure (Simplified from van den Dries et al., 2013). Podosomes consist of an f-actin core and adaptor proteins, e.g., talin, paxillin, and vinculin. The integrins are connected to the actin core via adopter proteins and protruded through the cellular membrane to sense its extracellular environment.

2.2.3 Osteoclast culture substrates for microscopic investigation

Early studies of OC *in vitro* were mainly conducted on glass (Marchisio et al., 1984) and bone (Chambers et al., 1984). OC morphology and behavior cultured on bone substrates differ from those cultured on glass, and OC expresses PDs on glass, but on bone it expresses SZ and RB (Bruzzaniti et al., 2005; Destaing et al., 2003; Luxenburg et al., 2007; Stenbeck and Horton, 2004). Therefore, it is highly desired to study bone resorption mechanisms on the bone surface. To study natural bone resorption of OC on bone, researchers have investigated the cells on thin slices of bone, dentin, or ivory using fluorescence confocal microscopy. However, due to the optical properties of bone, high scattering and autofluorescence, optical investigation of OC on bone has remained challenging. Even with relatively modern systems, actin bundles were not resolved in SZ and PD rings were barely distinguished from SZ due to the degradation of

the optical resolution (Szewczyk et al., 2013).

Alternatively, researchers have developed bone mimicking substrates with better optical properties, higher transparency and minimal autofluorescence. The coatings were calcium carbonate, hydroxyapatite, apatite-collagen complex, vitronectin, titanium, and calcite crystals (Brinkmann et al., 2012; Fuller et al., 2010; Geblinger et al., 2010; Redey et al., 1999; Shibutani et al., 2000). However, among studies on bone mimicking substrates, there are contradicting results. It was shown that mineralized coating promotes SZ formation, but not on a collagen substrate suggesting that OC recognition of minerals promotes bone resorption (Saltel et al., 2004). On the other hand, another study suggested that instead of minerals, vitronectin activates OC bone resorption (Fuller et al., 2010). These studies indicate strongly that OC research on bone is necessary and essential for the understanding of bone resorption mechanisms. Therefore, development of an osteoclast culture environment that facilitates both natural OC resorption and high-resolution optical imaging is desired.

2.2.4 Investigation of osteoclast actin cytoskeleton by optical microscopy

Electron microscopy provides ultra-high spatial resolution and good contrast on membrane structures in biological samples. Using electron microscopy in osteoclast studies, researchers resolved complex membrane structures in RBs at bone resorption pits and hypothesized that RB is the actual resorptive apparatus (Salo et al., 1997; Stenbeck, 2002). However, in electron microscopy, visualization of 3D actin structures together with associated proteins is difficult especially with an appropriate field of view. In addition, electron microscopy is mainly used for fixed samples, and imaging dynamics in live samples is a challenge. Fluorescence microscopy has provided many biological insights in bone biology. For example, Salo et al. visualized subcellular transcytosis routes of resorption products (Salo et al., 1997), Mulari et al. found subdomains of RB (Mulari et al., 2003), and Saltel et al. demonstrated dynamics of SZ on apatite collagen surfaces (Saltel et al., 2004). However, because the resolution in those studies were limited by the diffraction of light, available spatial information from fluorescence microscopy was limited.

Some studies showed AP (actin cloud) structures inside of SZ, and from the confocal axial view, the presence of f-actin was confirmed at

the bone surface (McMichael et al., 2010; Szewczyk et al., 2013). The authors claimed that the AP was associated with vesicular transcytosis at RB. However, due to the limited optical resolution the detailed structure of filamentous actin within the APs were not visible. Moreover, as bone resorption extends in 3D, axial localization of actin cytoskeleton at resorption site is as important as lateral extent. However, due to inferior axial resolution, their data barely showed relative axial position of the AP to SZ, but not axial details.

Nowadays, super-resolution fluorescence microscopy is widely used in biological studies. It was demonstrated that two-color STED microscopy partly uncovered the structure of podosome protein complex by analyzing vinculin binding angles around podosomes at the resolution beyond the diffraction-limit (Walde et al., 2014). However, the STED system provided super-resolution only in two dimensions, therefore, axial information in the study was limited. In comparison, iPALM have visualized protein assemblies of focal adhesion complexes at 3D super-resolution (Kanchanawong et al., 2010) revealing axial distribution differences among the proteins. From the acquired images, the group suggested axial protein localization in the focal adhesion protein complex. The study demonstrated a potential of 3D super-resolution microscopy in biological studies. However, iPALM utilized two opposing objective lenses and it implies a challenge in imaging biological samples on specific substrates.

As mentioned before, the actin cytoskeleton is assumed to be involved in transcytosis during bone resorption, and revealing nano-structures of actin filaments at AP as RB would provide more information to support the hypothesis of the f-actin involvement in the vesicular transcytosis. This promotes an application of the 3D super-resolution technique at the bone resorption site of OC.

3 AIMS OF THE STUDY

The aim of this doctoral study was to realize 3D super-resolution optical tomography utilizing a commercially available Leica TCS STED (SP5) microscope (I) on a newly developed, super-resolution compatible, bone-mimicking substrate (II) in a study of osteoclast bone resorption (III).

The Leica commercial STED microscope enables optical super-resolution, which is beyond the diffraction-limited resolution, but only in two dimensions. By employing tomographic STED microscopy, we have extended the 2D super-resolution system into 3D super-resolution and investigated axial details of cellular structures at 3D super-resolution (I).

Osteoclasts develop resorption machinery at a ruffled border (RB) on the bone surface, and the actin cytoskeleton is expected to be involved as a key player in this process. Due to the challenging optical property of bone, the details of actin cytoskeleton in OC in a natural environment have not been revealed optically before. To facilitate super-resolution imaging of natural-like bone resorption, a bone powder coating method on a microscope coverglass was developed. Super-resolution imaging of the bone resorbing osteoclast was demonstrated for the first time on a newly developed substrate (II).

In order to investigate the 3D nano-structures of f-actin at bone resorption site with fluorescence microscopy, the above-mentioned 3D super-resolution tomographic STED technique was applied at the site of bone resorption on the bone coated substrate (III).

In brief, aims of this study are:

1. Improving axial resolution of a commercially available STED microscope by tomographic microscopy, enabling 3D super-resolution STED microscopy (I).
2. Developing a bone powder coating method to facilitate super-resolution optical investigation of osteoclast cultured on bone surface (II).
3. Visualizing and analyzing actin cytoskeletal nano-structures at 3D super-resolution at the site of bone resorption, in order to provide an indication about the role that the actin cytoskeleton plays during bone resorption (III).

4 MATERIALS AND METHODS

This chapter summarizes materials and methods employed in this study. For more details, original publications should be referred (I - III).

4.1 Sample preparation

4.1.1 Fluorescent nanoparticles

As a point source calibration sample for tomographic STED microscopy, fluorescent nanoparticles (LifeTechnologies FluoSphere, 0.02 μm, Crimson Fluorescent) were used. For creating 3D distributions, the particles were deposited on fixed HeLa cells cultured on a microscope coverglass and mounted in 99 % 2,2′-Thiodiethanol (TDE) following a protocol by Staudt et al. (Staudt et al., 2007).

4.1.2 Bone coating and osteoclast cell culture

Cortical human bones from three different donors were mechanically pre-ground to produce millimeter scale powder. The pre-processed bone was further milled in an ethanol suspension with a planetary ball mill (Fritsch Pulverisette 6, Idar-Oberstein, Germany) to reach a particle size of 10-1000 nm to produce a smooth coating. Sedimentation was used to isolate bone particles in the range of 10-200 nm for coating. The milling balls used were 2 mm diameter ZrO_2 particles from Retch (Haan, Germany). After milling, the bone particle suspension was allowed to sediment for 2 hours. After the first sedimentation step, the supernatant was taken out and allowed to sediment for 16 hours. Only the fraction of particles remaining in suspension was used for the coating step.

For bone coating on a microscope coverglass, a cleaned coverglass was coated with poly-L-lysine by incubating in 0.01 % poly-L-lysine solution (Sigma-Aldrich Corporation, St. Louis, USA, P1524) overnight. Then, the coverglasses were coated with bone particles in buffer with 10 mM PO4, 0.025 % (w/v) Triton X-100, and 0.05 % (w/v) BSA. Finally the bone coating was fixed with 4 % paraformaldehyde (PFA) for 20 minutes, washed with water, and stored at 4°C.

In this study, two types of OC cultures were utilized: OC cultures were

established from human peripheral blood, and secondly, from human bone marrow-derived CD34+ stem cells (Lonza, Walkersville, USA). Blood-derived human OC cultures from peripheral blood of healthy volunteers were performed as previously described (Heervä et al., 2010). Briefly, the monocyte fraction was isolated with Ficoll gradient centrifugation according to the manufacturer's protocol. Then cells were seeded to coverslips and differentiated to multinuclear OCs in the presence of medium containing alphaMEM (GIBGO, Grand Island, NY, 41061-029), 10 % iFBS (GIBCO, Grand Island, NY, 16000-044), 10mM HEPES (Sigma-Aldrich, H0887), 1:100 penicillin-streptomycin, RANKL (20 ng/ml, Peprotech, Rocky Hill, NJ, 310-01) and M-CSF (10 ng/ml, R&D systems, Minneapolis, MN) for 8-10 days. Half of the medium was changed fresh after 3 to 4 days in order to preserve auto- and paracrine signaling molecules. Human bone marrow-derived CD34+ stem cells were suspended in culture medium and allowed to attach to the glass, bone slice, or functionalized glass surfaces. The culture medium (containing 10 % FBS, OCP BulletKit® Lonza, Walkersville, USA) was supplemented with 33 ng/ml M-CSF and 66 ng/ml RANK-ligand (OCP BulletKit® Lonza, Walkersville, USA). After completion of osteoclast differentiation at day 7, all culture medium was removed and fresh medium was added into the wells. The mature osteoclasts were cultured for an additional 3 days, allowing them to resorb bone.

4.1.3 HeLa cell and osteoclast immunostaining

To demonstrate tomographic STED microscopy in a biological sample, HeLa cells, cultured on microscope coverglass, were labeled with fluorescent molecules for microtubules. HeLa cells were fixed with 4 % PFA for 20 min, permeabilized with 0.2 % Triton X-100 for 20 min, blocked with 5 % BSA and 0.1 % Triton X-100 for 45 min, treated with primary anti-α-tubulin antibody (Sigma-Aldrich Close AA13, lot 120M4771) at 1:100 dilution in 1 % BSA with 0.1 % Triton X-100 for 1 hour, and treated with secondary anti-mouse antibody conjugated with Atto647N (ATTO-TEC, Germany) at 1:100 dilution in the same solution for 1 hour. Finally cells were mounted in TDE for tomographic STED microscopy following a protocol by Staudt et al. (Staudt et al., 2007). All the incubations were conducted at room temperature.

For imaging bone resorbing OCs, cells cultured on bone coated

coverglass were labeled with one of the following primary antibodies: anti-dynamin antibody (BD Biosciences, Clone 41/Dynamin catalog No. 610245), rabbit anti-arp2 antibody (abcam, ab47654), or rabbit anti-V-ATPase antibody (Santa Cruz Biotechnology, sc28801) followed by corresponding anti-mouse or anti-rabbit antibodies conjugated with Alexa Fluor 488 (LifeTechnologies, U.S.A.) and phalloidin conjugated with Star635 for f-actin (Abberior, Germany). Cells were mounted in water.

For imaging bone resorbing OCs with tomographic STED microscopy, cells cultured on bone coated coverglass were labeled for f-actin following the above mentioned protocol but with primary anti-f-actin antibody (Bioss, bs-1571R) at 1:100 dilution and secondary anti-mouse antibody conjugated with Star635P (Abberior, Germany) at 1:100 dilution. Cells were mounted in TDE following a protocol by Staudt et al. (Staudt et al., 2007).

4.2 Instrumental setup

4.2.1 Microscopic settings

For imaging the calibration nanoparticles, an excitation wavelength of 635 nm and a depletion wavelength of 735 nm were used, and the fluorescence signal was detected with an avalanche photo diode (APD) using a detection bandwidth of 665 – 705 nm. For imaging α-tubulin stained HeLa cells with Atto647N, the same excitation laser and detection bandwidth were used as the calibration sample, but the depletion wavelength was changed to 770 nm. For imaging OCs on a bone surface labeled with Star635P, an excitation wavelength of 635 nm and depletion wavelength of 760 nm were used and the emitted fluorescence was detected with an APD a detection bandwidth of 665 – 705 nm. Exceptionally, the depletion wavelength was set to 735 nm in case of tomographic STED microscopy on a bone surface in order to gain better depletion efficiency with lower power. Alexa Fluor 488 was excited at 488 nm and fluorescence was detected with a photomultiplier tube (PMT) using a detection bandwidth of 500 – 560 nm. To visualize topography of the bone surface, a reflection light from 476 nm was detected with PMT at a detection band of 460 – 475 nm. Image pixel size was set to 20 – 25 nm, satisfying Nyquist criterion for the microscope used, and a line scan speed of 700 Hz with line averaging of 8 or 16 were used. Z-stack images were acquired

with a step size of 250 nm.

4.2.2 Tomographic STED microscopy

For tomographic STED microscopy of the fluorescent nanoparticles and HeLa cells labeled for α-tubulin, atomic force microscope (AFM, Agilent 5500 SPM, Agilent Technologies, USA) was coupled to the STED microscope. A commercially available gold-coated AFM chip with the cantilever removed (CSC17 Cr-Au and NSC35 tipless Cr-Au, Innovative Solutions Bulgariz, MikroMasch) was attached to the AFM with an angle spacer and was used as a micro-mirror (see Figure 9). The chip itself was used for the purpose since it formed a high quality mirror surface. The mirror was manually set to a horizontal angle between 20 and 30 degrees, and the angle was determined from the acquired images during image processing. After mounting a sample, the micro-mirror was positioned close to a ROI using the AFM (Publication I). As a further simplified development, a custom-built manual x-y-z translational stage was used as a micro-positioner with a custom mirror for imaging of the osteoclasts on bone coating surfaces (Publication III). The angle of the mirror on the manually operated holder was determined similarly to the AFM mounted mirror from the acquired images. The coated mirrors for the simplified setup were provided by Dr. Pääkkönen in Prof. Honkanen's group, UEF, Finland.

4.3 The protocol for tomographic STED microscopy

For tomographic STED microscopy, a sample was imaged at two different angles: one taken from below (*bottom view*) and another taken via a mirror (*side view*) (Figure 9). The bottom view was acquired with normal imaging, and the side view was acquired by focusing deeper via the mirror to the same ROI. The observation angle was dependent on the manually positioned mirror angle, which was horizontal angle between 20 to 30 degrees. The re-focusing took between a few tens of second to a minute for finding a mirror in a field of view in the reflection channel and focusing deeper for 15 - 40 µm. In typical setting and samples, the bottom view required 10 to 20 slices and the side view 20 to 40 slices. Due to the flat proportions of cells, the side view required usually more slices.

The acquired two 3D stacks, from the bottom view and side view, were reconstructed with either manual or computational registration into a 3D tomogram containing super-resolution in all three dimensions. The reconstruction with computational registration was done by a custom-written software by Koho et al. and detailed parameters and settings can be found in the work (Koho et al., 2015).

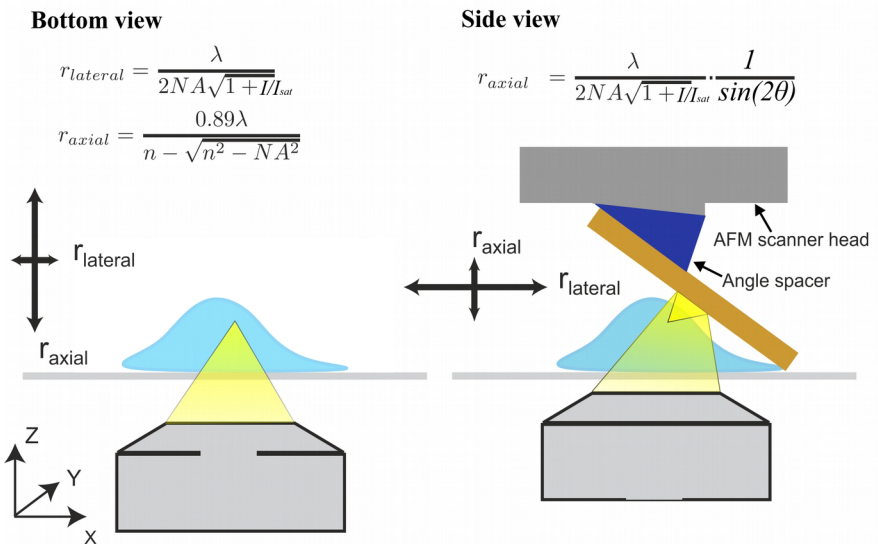

Figure 9: Tomographic STED microscopy setup. The same region in a sample is imaged at two different angles. The bottom view is acquired from normal imaging and side view is acquired via a mirror placed on top of the sample. The mirror was attached to the AFM and its angle was adjusted with an angle spacer. The arrows represent the resolution in each of the views. In the side view, axial resolution depends on the mirror horizontal angle, θ. (Modified from Publication I)

5 RESULTS AND DISCUSSION

We have realized 3D super-resolution tomographic STED microscopy on a commercially available 2D super-resolution Leica STED microscope (I). To facilitate super-resolution imaging of osteoclasts (OC) on a bone surface, a bone coating method on microscope coverglass was developed (II). These two techniques were applied together to visualize nano-structures of actin cytoskeleton at 3D super-resolution at a bone resorption site within OC (III).

5.1 Tomographic STED microscopy (I)

Tomographic STED microscopy was first demonstrated on fluorescent nanoparticles and microtubule-stained HeLa cells (I).

Firstly, 20 nm fluorescent nanoparticles deposited on cell surfaces were imaged using tomographic STED microscopy. For acquiring a view from the side of the target, a commercial gold-coated AFM chip was set close to a ROI. Because the chip itself had a larger area and higher quality surface than the cantilever, the cantilever was removed and the chip surface itself was used as a mirror. The ROI was imaged from two angles, one from below (*bottom view*) and another via the mirror (*side view*). In this setup, with a mirror horizontal angle of 30 degrees, the side view created approximately 60 degrees in relation to the bottom view. As shown in Figure 9, the axial resolution depends on the horizontal mirror angle. Z-stack images were acquired from the two views, manually registered in 3D space, and fused into a single 3D tomogram. The fusion process was based on logical AND operation in which only colocalizing pixels between the two views were taken into the tomogram. The system was capable of resolving two separate nanoparticles 75 nm apart in the bottom view (Figure 10 b and c) and 85 nm in the side view (Figure 10 d and e), demonstrating super-resolution in both views. In the final tomogram, the system resolved two nanoparticles that were 90 nm apart along z-axis, which successfully demonstrated 3D super-resolution (Figure 10 g and h). Compared to the previous studies (Heintzmann and Cremer, 2002), we have succeeded obtaining nearly isotropic resolution in tomographic microscopy only with two views.

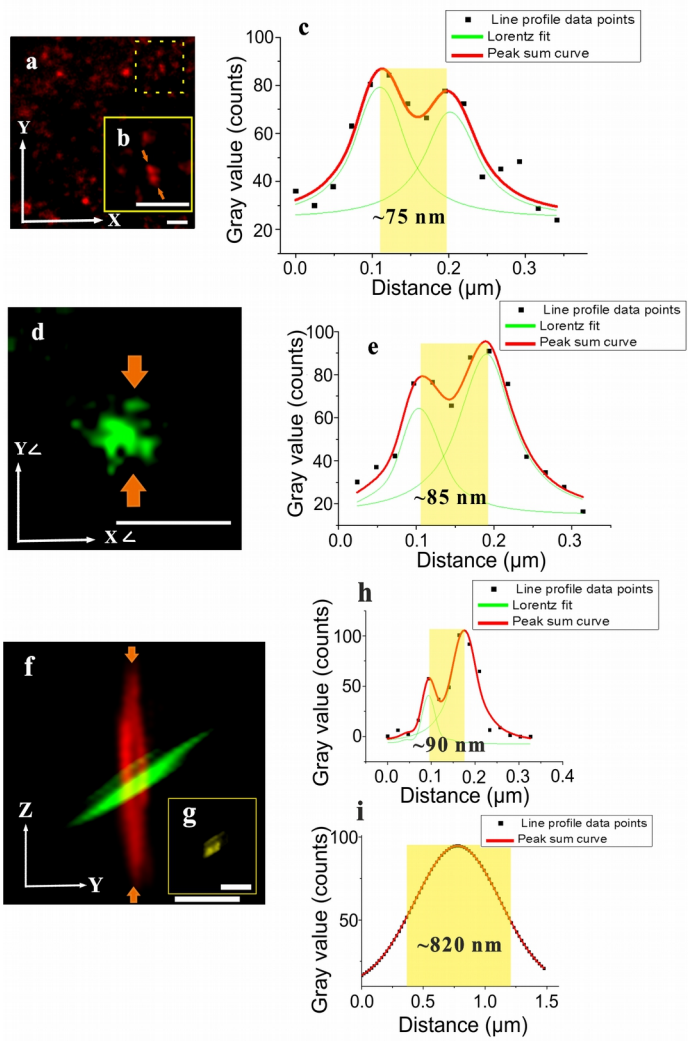

Figure 10: Tomographic STED microscopy on nanoparticles. Bottom view image shows two closely located nanoparticles were resolved (a, b). (c) Intensity line profile taken at arrows in (b) showed two separate peaks, which were 75 nm apart. (d) Side view shows one nanoparticle separated from a large cluster of nanoparticles. (e) Intensity line profile taken at arrows in (d) showed two separate peaks, which were 85 nm apart. (f) Y-Z cross sectional image from two registered and overlaid stacks, where bottom view in red and side view in green. (g) The extracted overlap volume from (f) showing a nanoparticle axially separated from a large cluster of nanoparticles. (h) The axial intensity profile of tomogram (black dots) taken at the orange arrows in (f). Clearly two peaks are separated with a distance of 90 nm. (i) In the corresponding axial intensity profile of bottom view Gaussian fit curve (red line) showed only a single peak with FWHM of 820 nm. Scale bar 500 nm in (a), 300 nm in (d) and (f). (I)

Secondly, HeLa cells labeled for microtubules were imaged with the tomographic STED microscopy to demonstrate the applicability of the technique in biological samples (Figure 11 a). With a horizontal mirror angle of approximately 23 degrees, the system revealed axial details that were beyond the diffraction-limited resolution. Statistical analysis of axial FWHM of microtubules in raw data was approximately 73 nm in the side view, and it demonstrated axial super-resolution (Figure 11 b and d).

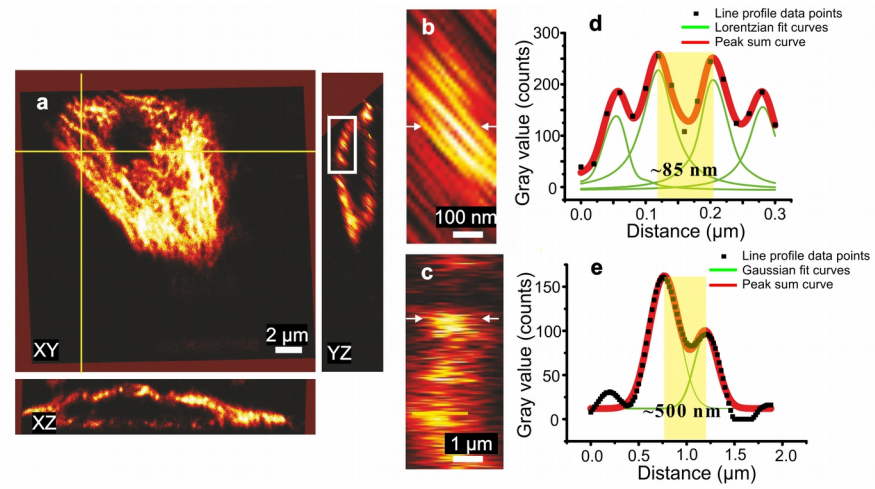

Figure 11: STED microscopy side view on HeLa cells. (a) Orthogonal views of microtubules are shown. (b) Enlarged side view image in Y-Z plane (square in a) shows PSF tilted at approximately 45 degrees with rich axial details. (d) Intensity line profile from (arrows in b) shows two peaks 80 nm distant were resolved (yellow shade). (c) Similar Y-Z image from normal bottom view shows PSF elongated in axial direction. (e) Intensity line profile from (arrows in c) shows two peaks 500 nm distant were resolved. Note that image (c) is not from image (a), but from similar location in a corresponding normal STED image. (I)

In our system, the achieved axial resolution was worse than the approaches with two objective lenses, such as isoSTED and iPALM (Schmidt et al., 2008; Shtengel et al., 2009). However, when compared to the axial resolution reported with single objective lens systems (Harke et al., 2008; Huang et al., 2008; Schermelleh et al., 2010), the

tomographic STED achieved better axial resolution.

As explained in Figure 9, axial resolution in side view depends on the mirror angle. Theoretically, the mirror angle of horizontal 45 degrees creates the side view perpendicular to the bottom view and will provide the best axial resolution in tomographic STED microscopy. However, a comparison of the resolution at the side view (85 nm) and the final tomogram (90 nm) on nanoparticle data did not show a significant resolution decline. With a mirror angle of 54.7 degrees instead of 45 degrees, Tang el al. achieved similar z-resolution to x-y resolution (Tang et al., 2010). Therefore, we hypothesized that the axial resolution degradation at the mirror angles used in our studies, which were smaller than 45 degree, is not significant because the elongation of the STED PSF is about one order of magnitude in comparison to the lateral size of the PSF. Importantly the equation for the axial resolution in side view (Figure 9) goes to infinite when the theta reaches zero degree. However, in our system, the theta was kept much greater than zero due to space constraint.

Another aspect of the mirror angle is its relation to the number of z-stack slices. A higher number of z-stack slices is needed as the mirror angle approaches to 45 degrees due to the flat proportion of the cells (Figure 5 a). And, at 45 degrees, imaging the sample surface with the side view becomes a challenge, because the optical path becomes parallel to the sample surface. Therefore, in our work, a smaller mirror angle was used.

Due to a lack of computational registration, the alignment of two 3D stacks with complex microtubule structures at high precision was not possible for the first publication. As a result (I), only the data from fluorescent nanoparticles was reconstructed into a final tomogram. However, a computational registration and fusion on the HeLa cell microtubule data was demonstrated in a recently published article (Koho et al., 2015).

5.2 Bone powder coating and super-resolution STED microscopy on osteoclasts (II)

5.2.1 Technical achievement

The developed bone coating method was applied to microscope coverglass and was evaluated for super-resolution optical imaging (II).

The bone coated coverglass was found to be semi-transparent (Figure 12 a), and from the x-z confocal reflection image, the coating was confirmed to be smooth and thin with approximately 7 µm thickness (Figure 12 b).

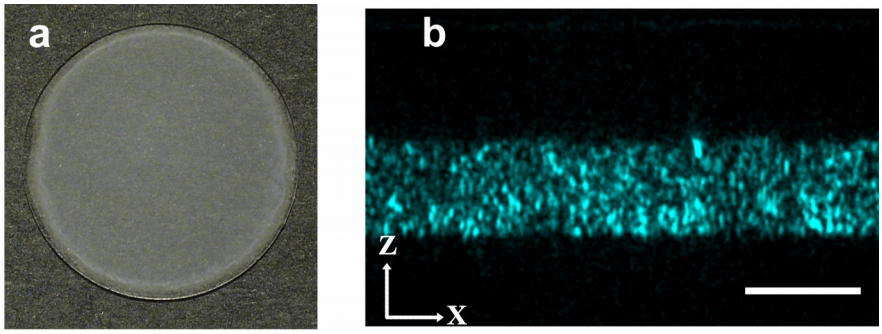

Figure 12: Bone coating on coverglass. Bone powder coating on microscope coverglass (a), and its cross-sectional reflection image (b) showing semi-transparent, smooth and thin bone layer. Scale bar 10 µm in (b). (II)

2D super-resolution fluorescence microscopy was demonstrated on a bone coated microscope coverglass (II). OC cultured on bone coating was labeled for f-actin with phalloidin-Star635P and imaged by STED microscopy. With the system, we measured a FWHM of 60 nm at a small actin structure (in raw data without any post-image processing), and this indicated that the system resolution is approximately 60 nm (Figure 13 d and e). Compared with the best resolution of the system on a calibration sample, which is approximately 55 nm, the resolution degradation from bone coating was small. F-actin bundles 140 nm apart were clearly resolved in the same image (Figure 13 e). In the confocal image, neither detailed filamentous actin structures nor the two peaks were resolved (Figure 13 a and e), and this demonstrates the optical resolution improvement by STED microscopy on the bone coating. A similar comparison was conducted on a bone slice, and STED microscopy did not show a good resolution improvement compared to the corresponding confocal image (Figure 13 f and g). These results demonstrate that bone coating improves the optical property of the substrate, generating less scattering and autofluorescence, and facilitates super-resolution microscopy, in comparison with the traditionally used bone slices.

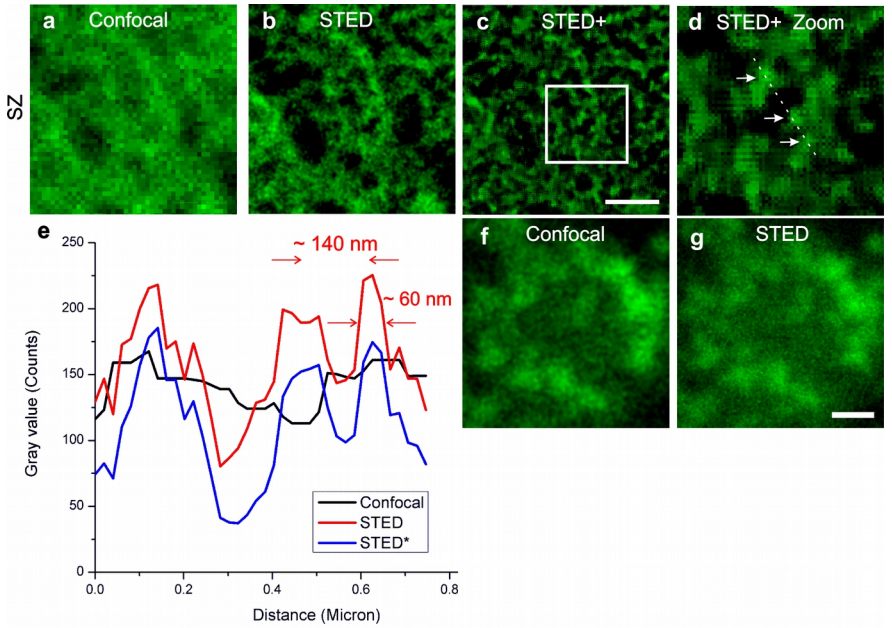

Figure 13: STED microscopy images of OC on bone coated coverglasses. A small area of a sealing zone (f-actin) by confocal (a), STED (b), and STED with deconvolution (c, STED+) are shown. (d) shows an inset from (c) demonstrating detailed f-actin network structures. (e) shows an intensity line profile from (d at line), in which a small actin feature with FWHM of 60 nm and adjacent peak with 140 nm distance are resolved by STED microscopy, while corresponding confocal data only shows a single peak. (f) is the confocal and (g) the STED images of a small f-actin ring on a bone slice showing a very limited resolution improvement. Scale bar 1 µm in (c) and (g). (II and unpublished data)

A high power STED beam (approximately 45 mW) was focused on the sample in a viscous mounting medium and caused sample damage from local heat generation. Considering that successful STED microscopy with 120 mW depletion laser power at focus has been reported (Vicidomini et al., 2014), the damage was caused because of the bone coating. However, we found that as a mounting medium, water served as a good heat exchanging component. This allowed, with maximum STED beam power, best available resolution and preservation of the sample.

Even with the expected resolution degradation from optical aberrations caused by the refractive index mismatch at the interfaces between coverglass and bone and bone and water (Gould et al., 2012), we did not experience drastic resolution degradation. This was assumed because firstly, the interesting events in OCs were on the bone surface and optical path in water was relatively short, and secondly, the smooth and thin bone layer (Figure 12 a, b) provided minimal distortion on the wavefront of excitation and depletion beams.

5.2.2 Biological achievement

To evaluate OC activities on bone coating, bone surface topography as well as OC f-actin structures were studied (II). On the coating, two types of OCs were cultured for 10 days and prepared for fluorescence microscopy. The sample with bone marrow-derived OCs showed a number of holes on the bone coating surface in reflection channel, as RPs (Figure 14 a). In f-actin channel, a large actin ring as SZ was observed (Figure 14 b). In merged channel, the SZ was confirmed surrounding one of the RPs (Figure 14 c). In the sample with blood-derived OCs, we again observed many RPs (Figure 14 d). In the f-actin channel, APs as RBs and small actin rings (SARs) were observed (Figure 14 e). In the merged channel, the actin signals were often colocalized with the RPs (Figure 14 f). Unlike similar studies conducted on bone slices (Szewczyk et al., 2013), f-actin bundles were clearly visualized in the acquired images demonstrating a good optical property of bone coating.

According to past studies (Chambers et al., 1984; Palokangas et al., 1997), those holes as RPs found with SZ and APs as RBs on bone surface (Figure 14 c and f) suggest strongly bone resorption by OCs. To further confirm OC resorption with direct evidence, c-terminal cross-linking telopeptides of type I collagen (CTX) were analyzed in the culture medium after 10 days of cell culture (data not shown) according to the protocol in (Heervä et al., 2010). The analysis confirmed a higher concentration of CTX in the cultured medium with OCs on bone coating, while very low concentration on bone coating without OCs. This result confirmed the presence of OC active bone resorption on the bone coating.

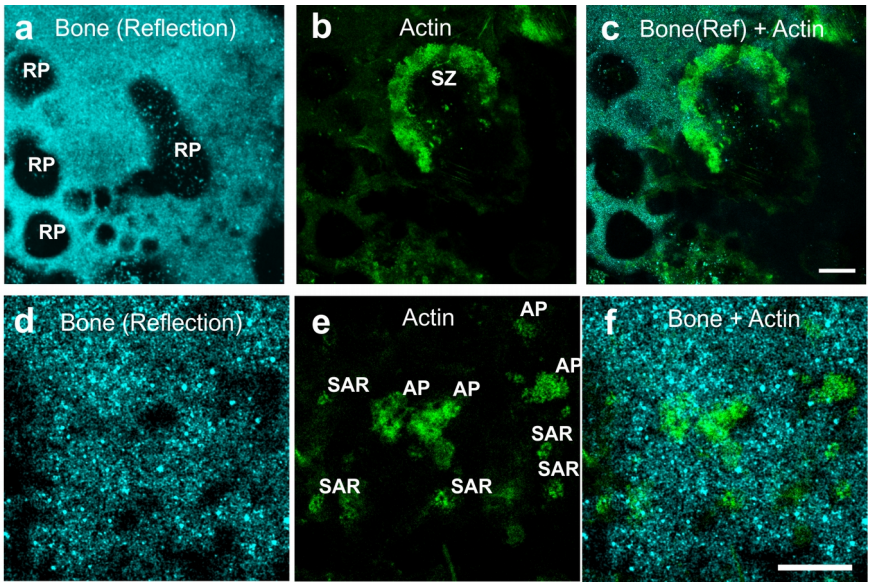

Figure 14: OC bone resorption on bone coated coverglass. (a-c) Within a sample with bone marrow-derived OCs, a number of RPs were found in reflection channel (a) with a sealing zone in fluorescence channel(b), which surrounded one of the RPs (c). (d-f) Blood-derived cells prepared with same protocol also showed RPs (d) with APs as RBs and small actin rings (e). Some of the APs were found colocalized with RPs. Scale bar 20 µm in (c) and (f). (II)

STED microscopy applied on SZ (Figure 15 a-f) and AP revealed (Figure 15 g-m) finer detailed filamentous network of dense actin (Figure 15 e, h) compared with confocal images (Figure 15 d, g). Especially in AP, the filaments were found forming bright puncta or ring-like shapes (Figure 15 h, i). A closer look of those structures showed intense f-actin with different degrees of connecting filament networks with varying sizes of around 100 nm (Figure 15 j-m).

Based on a study by electron microscopy (Collins et al., 2011), those structures of circular shaped f-actin may indicate the presence of vesicles surrounded by actin filaments for endocytosis, at which f-actin may form comet-tails and can generate forces to support budding endosomes for scission and further transportation. To the best of our knowledge this was the first time that the circular shaped f-actin structures were visualized in bone resorbing OC. The indication of f-actin involvement during done resorption needs to be confirmed by visualizing f-actin with vesicles stained for V-ATPase and resorption

products as well as visualizing comet-tails with Arp2/3 complex.

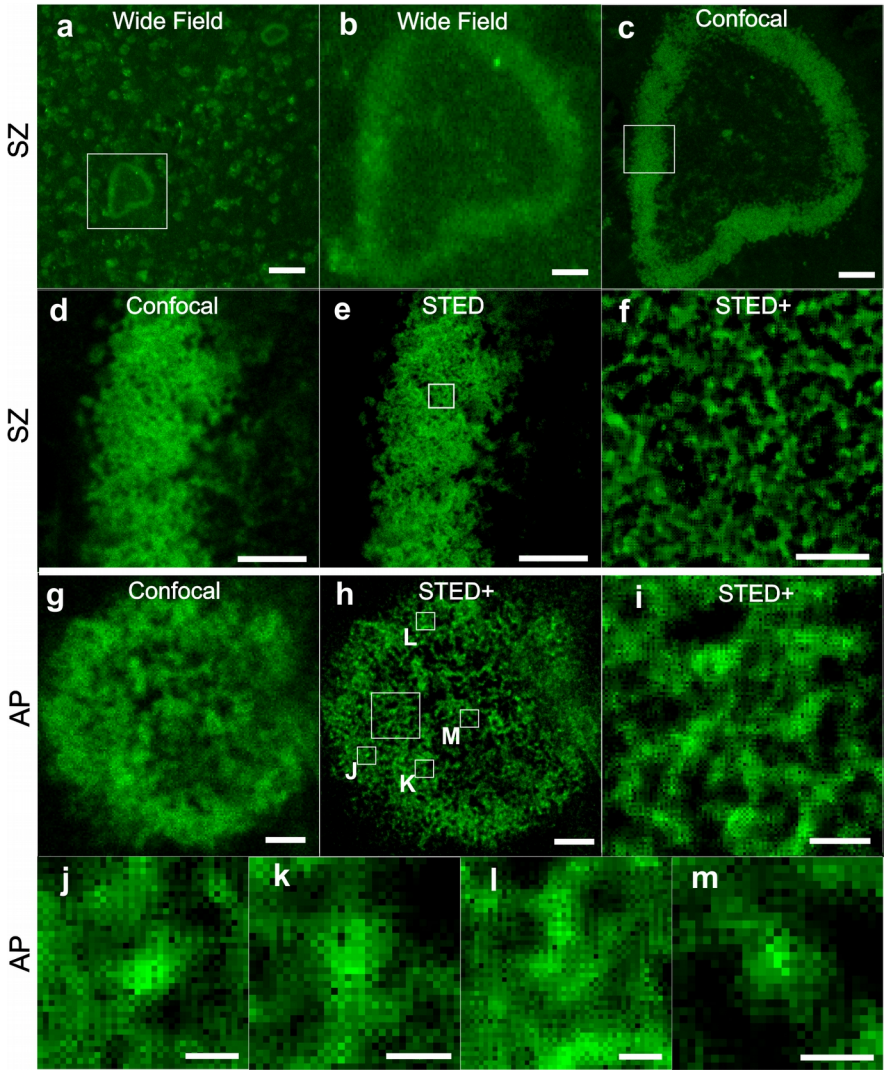

Figure 15: Examination of SZs and APs at 2D super-resolution. (a - f) SZ-structure at different magnifications with widefield (a and b), confocal (c and d) and STED (e and f) microscopy (f with deconvolution). SZ showed a uniformly dense f-actin with a closely-knit structure. (g - m) AP structure with confocal (g) and (h and i) with STED showed an f-actin network structure with occasional brighter puncta (i). Zoomed in STED images with deconvolution (j-m) showed bright puncta with occasional circular shape that might correspond to endocytosis events with surrounding f-actin. Scale bar 50 µm in a, 10 µm in b and c, 5 µm in d and e, 1 µm in f, 2 µm in g-h, 0.5 µm in i, 0.2 µm in j-m. (II)

In combination with f-actin, two other proteins representing events related to resorption and associated with f-actin and endocytosis were imaged. One of those proteins, dynamin was to localize endocytotic events, and another, Arp 2/3 complex to localize f-actin nucleation and branching as a sign of force generation. Dynamin was found to strongly colocalize with f-actin in AP (Figure 16 a-c). At the AP, f-actin bundles were found colocalizing well with filamentous distributing dynamin (Figure 16 h). Arp 2/3 complex was also found to strongly colocalize at AP nearby a RP (Figure 16 e-g).

In our results, both dynamin and Arp 2/3 complexes were colocalized strongly with f-actin at APs, and this suggests that RB is present at the APs and endocytosis events and vesicular transports by generated force from branching f-actin are ongoing. Based on the past studies about dynamin (Mulari et al., 2003; Praefcke and McMahon, 2004) and Arp complex (Collins et al., 2011), the presence of active bone resorption and f-actin involvement at the APs as RBs are suggested.

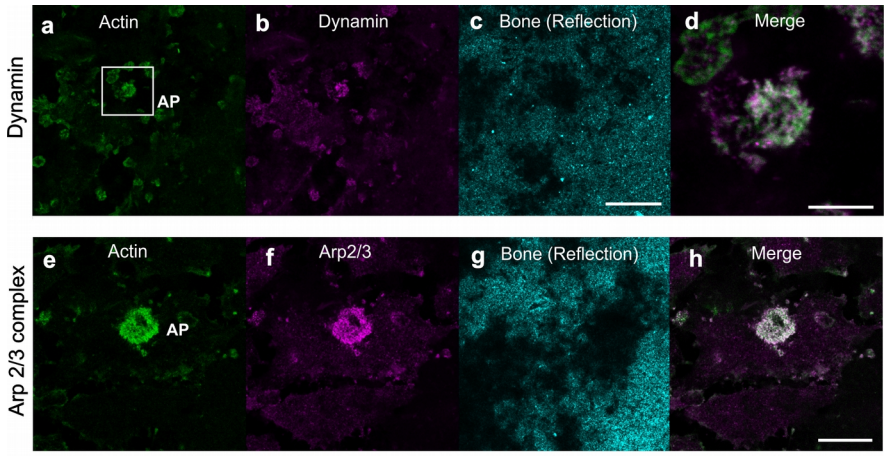

Figure 16: Dynamin and Arp 2/3 complex at AP. (a - d) RP (c) coincided with AP structures exhibiting a network of filamentous actin (a) and dynamin (b) staining. (a) Actin at AP structures was organized in form of intensely stained discs of networked actin with a number of bright puncta. (b) Dynamin showed an intense staining at AP structures, indicating specific accumulation at these zones and vesicular endocytosis. (d) An overlay image of dynamin and actin shows dynamin localizing at the puncta in actin network. (e - f) AP structure of f-actin (e) that shows an intense Arp2/3 staining organized in filaments (f) near a large RP (g). In merged image (h), despite of considerable overlap, all actin signal does not fully colocalize with Arp2/3. Scale bar: 5 µm in (d), 20 µm in (c) and (h). (II)

5.3 3D super-resolution structures of actin cytoskeleton at bone resorption site (III)

5.3.1 Technical achievement

Tomographic STED microscopy was applied to investigate 3D extent of actin cytoskeleton at 3D super-resolution (III). An area with complex networking f-actin with RP in reflection channel was found in a sample with OC cultured on bone coating. The AP like f-actin was considered as RB, and the area was selected as a bone resorption site and imaged with tomographic STED microscopy (Figure 17 a). The area was imaged at two angles, one from below and another via a mirror, which was set at horizontal angle of 29 degrees. The two views were reconstructed into a tomogram with computational registration

and fusion, according to a protocol by Koho et al. (Koho et al., 2015). The depletion laser wavelength was set at 735 nm with 4.5 mW of laser power measured at the focus.

In the bottom view, a comparison of confocal and STED images showed approximately a two-fold improvement in lateral FWHM (Figure 17 b, c, and i). In the tomogram, the demonstrated resolution improvement in axial direction was approximately 210 nm, which was two times better when compared to the diffraction-limited resolution (Figure 17 e and j). Therefore, considering the wavelength used, the final tomogram was 3D super-resolution image.

Since the side view via a mirror has a longer optical path in a sample, refractive index mismatch causes severe optical aberrations in the view. Because of this, tomographic STED requires a precise refractive index match between objective lens immersion and mounting media. This fact did not allow us using water as mounting medium in this setup. To avoid sample damage from a high power STED beam, approximately 4.5 mW at the focus, which is only 10 % of available beam power, was used. To compensate for resolution decline from the reduced STED laser intensity, the depletion wavelength was shifted from typically used 770 nm to 735 nm for higher depletion efficiency. With these settings, we achieved axial resolution of approximately 210 nm. For further resolution improvement, viscosity of mounting medium needs to be decreased without compromising its refractive index.

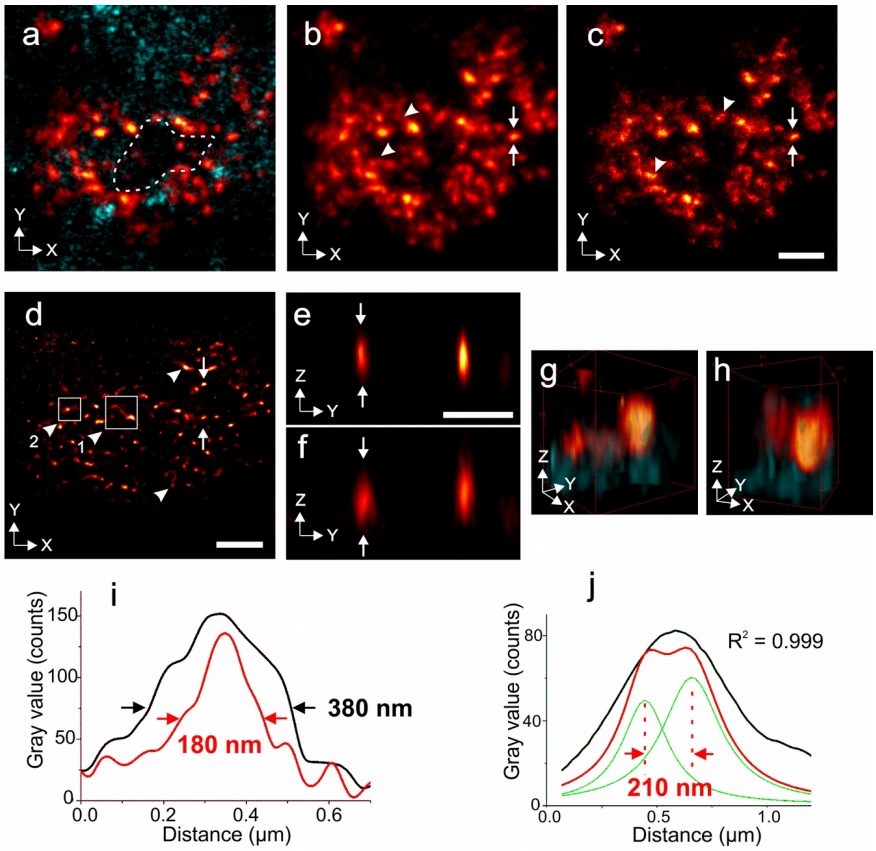

Figure 17: Tomographic STED microscopy on bone resorbing OC. (a) A single confocal section with bone reflection signal (cyan) and complex f-actin as AP (red) shows actin surrounding an empty area on bone (broken circle in a) suggesting a RP and a RB. Maximum intensity projection (MIP) image of the AP by STED microscopy (c) shows more details than the corresponding confocal image (b). (i) Intensity line profile of STED (red) from raw data shows FWHM (from arrows in b) is about half of the corresponding confocal (black) showing resolution improvement. (d) A MIP image of tomographic STED with comet-tail like shapes indicated by arrowheads. (j) A line profile (red in j) of STED tomogram (from e) shows clear double peaks that are 210 nm apart while corresponding profile (black in j) from normal STED (from f) showed only a single peak. (g) and (h) are 3D snapshots taken at arrowheads (1) and (2) in (d), respectively, showing comet-tail f-actin structures with upwards and downward orientations indicating endo-/exocytosis events. Scale bar 2 µm in c and d, 1µm in e. (III)

5.3.2 Biological achievement

The visualized f-actin structures at 3D super-resolution in bone resorbing OCs were analyzed (III). In the final tomogram, a number of f-actin comet-tails was found (Figure 17 d). The comet-tails were found very close to the bone surface (Figure 17 g, h) within several hundreds of nanometers. With the nanoscale axial features resolved at super-resolution, orientations of the comet-tails extending for 100 – 300 nm in axial direction were visualized. Some of the comet-tails were directed downwards and some upwards (Figure 17 g and h, respectively). The comet-tails suggest branched f-actin polymerizing around vesicles (Cameron et al., 2001; Svitkina, 2013). In past studies, the presence of exocytosis of vesicles to resorption sites and endocytosis of vesicles containing resorption products from resorption sites to FSD were suggested (Nesbitt and Horton, 1997; Salo et al., 1997; Teitelbaum, 2000). According to those studies, the downwards and upwards oriented comet-tails may suggest an existence of the following events. The comet-tails directing toward the bone surface may be carrying acidified vesicles with proteases for exocytosis to the resorption area, and comet-tails directing away from the surface may be carrying vesicles formed from endocytosis of resorption products.

Based on the previous studies (Hirvonen et al., 2013; Mulari et al., 2003), the orientations of the comet-tails were expected to be area specific, because more comet-tails going upward to be found at the center, and the downwards counter-parts were located at the peripheral area of the RB. However, our data did not support this specificity. One reason could be that the RB in our data is approximately 10 μm in size, which is several times smaller than the ones in those previous studies. We could hypothesize that a larger RB has more area specificity for exocytosis and endocytosis.

5.4 Advantages and considerations of tomographic STED microscopy

One of the benefits of our tomographic STED microscopy that is based on a micro-mirror is its applicability to be utilized without modifying the optics, in, e.g., commercial systems. Compared to past studies, such as those using iPALM and isoSTED, which have been implemented on custom-build systems, the flexible applicability is the benefit of our approach.

Another advantage of the tomographic STED microscopy is the nearly isotropic resolution provided efficiently with a single objective lens. According to a computational modeling (Mark et al., 2015), unlike the lateral depletion beam (lateral doughnut), the axial depletion beam (axial doughnut) had a non-zero center, which could result in inefficient use of the depletion beam and lower signal-to-noise ratio (SNR). The authors also indicated that an axial-doughnut is more prone to refractive index change, and when imaged through a nucleus it can be distorted up to an order of magnitude more than lateral-doughnut. The distortion caused positional shift of intensity minima occurred relative to the excitation beam, which implied a decline in resolution. The tomographic STED microscopy utilizes the lateral-doughnut in all directions for resolution improvements, thus it is efficient in achieving nearly isotropic super-resolution; the system achieved less than 100 nm 3D resolution with 45 mW in a pulsed laser system.

Furthermore, it requires a lesser sampling rate because it obtains only 2D super-resolution information from each scan. Unlike other 3D super-resolution techniques (Schmidt et al., 2008), tomographic STED acquires super-resolution information only in two directions at each view. This reduces sampling frequency in one direction and the subsequent faster imaging prevents photobleaching and reduces heat buildup in the sample. However, it should be noted that both the axial resolution and the number of side view images for a 3D stack depends on the mirror angle and they are a trade-off of each other. Therefore, a researcher is advised to optimize the mirror angle according to a purpose of each experiment.

A benefit of our technique compared to the tomography with sample rotation in practical manner is its applicability. Unlike the sample rotation approach (Heintzmann and Cremer, 2002; Saux et al., 2009), the second view is obtained via a mirror and thus the sample itself is not rotated. Therefore, no specific sample preparation, e.g., cells grown in a thin glass pipette, is required, and hence our method allows standard cell culture protocols to be used and provides more freedom of biological sample preparation.

In the tomographic STED system demonstrated in this work, the number of views was limited to two. It was demonstrated that the resolution and image contrast in tomograms increased with a higher number of views (Sätzler and Eils, 1997). However, super-resolution information of fluorescent molecules in three axis can be acquired only

from two views: the bottom view acquires in x-y and the side view in y-z (Tang et al., 2010). And it was demonstrated that improved reconstruction algorithms enhanced resolution in a tomogram with fewer number of views (Heintzmann and Cremer, 2002). Therefore, for a tomographic reconstruction, only two views would theoretically be enough to generate isotropic 3D resolution with the available lateral resolution. In general, super-resolution images are noisy with low SNR. Because the noise is expected to distribute differently in each view, increasing the number of observation angles together with improvements in the reconstruction algorithms can possibly improve the resulting image contrast in our technique. However, this is beyond the scope of this thesis but worth mentioning for further improvements in tomographic STED microscopy.

6 CONCLUSIONS

We have developed a 3D super-resolution system, tomographic STED microscopy, based on a commercial microscope with 2D super-resolution (I). The technique was realized by having two oblique observation angles using a micro-mirror, followed by reconstruction of the two views into tomogram and demonstrated nearly isotropic resolution less than 100 nm.

To study bone resorbing OC with super-resolution STED microscopy, we developed a cell culture environment (II) that facilitates natural-like bone resorption and optical imaging at super-resolution. The culture environment was realized by coating a microscope coverglass with bone powder and forming a smooth and thin layer of bone. Images acquired on the bone coating revealed nano-structures of circular shape and puncta of actin cytoskeleton at AP as RB in bone resorbing osteoclast at super-resolution.

To study 3D structures of OC actin cytoskeleton at bone resorption site, the two above mentioned techniques were combined and applied on human osteoclast (III). As a result, we have visualized the actin cytoskeleton at the site of bone resorption at 3D super-resolution. The reconstructed tomogram showed the specific f-actin structure, comet-tails, which indicated force generating branching filaments. The acquired data suggests an involvement of f-actin in vesicular exo-/endocytosis in bone resorption, a role for the actin cytoskeleton in the regulation of exocytosis of resorption associated proteins and enzymes, and endocytosis of resorbed bone products.

As a conclusion, for the first time, this present study of 3D super-resolution technique with a combination of bone coating method has revealed fine detailed actin structures in bone resorbing OC (III). The acquired results have brought a new perspective into bone biology. F-actin may play a key role in exo-/endocytosis in bone resorption. This demonstrated the system capability for better understanding biological mechanisms by resolving finer structures at 3D super-resolution.

7 ACKNOWLEDGEMENTS

The thesis was carried out in the Laboratory of Biophysics, Department of Cell Biology and Anatomy, Institute of Biomedicine and Medicity Research Laboratories, University of Turku. International Doctoral Programme in Biomedical Engineering and Medical Physics (iBioMEP) and Turku Doctoral Programme of Molecular Medicine (TuDMM) are acknowledged for a full-funded doctoral student position. European Science Foundation and Academy of Finland are acknowledged for research funding.

I would like to express my greatest gratitude to my primary supervisor, Professor Pekka Hänninen. With your decision of taking me to your group, I could started pursuing a degree in this interesting research field. You have given me a large freedom so that I could explore the field freely and come up with unique ideas. I always appreciated and respected your supervision policy. And to my second supervisor, Doctor Tuomas Näreoja, another great gratitude goes for your dedicated guidance and instructions with a lot of enthusiasm and confidence.

I wish to thank the preliminary examiners, Professor John Eriksson and Professor Thomas Klar. Both of you provided great scientific insights to improve this thesis within a very limited time. I would like to thank my follow-up committee members, Professor Peltonen, Docent Soini as well as Docent Härma, for valuable advice. I also would like to acknowledge, Outi, Sonja, Eeva, Nina, as well as Elina, Petra, and Iiris for their administrative supports.

I wish to thank all my coauthors for their support to the publications. Especially Tuomas, Sami, as well as Professor Peltonen and his group members, Maria, Paula, and Miso are warmly acknowledged. Professor Honkanen, Pertti, Hannu, Hannu-Pekka are acknowledged for their supports in mirror fabrications. Co-authors in other publications and collaboration projects during my doctoral study are acknowledged. Especially Professor Larsson and Meishan for wonderful myosin work; Professor Rosenholm and Neeraj for the graphene work; Professor Shupliakov, Åsa, Kathryn, Annika and Anna

for exciting fly synapse project; Katja, Miso, and Soili for OC projects; and Sirkku, Roope K., Jussi, Tiina, Meraj, Helen, Markus, Rose, Konstantin and Olga for other interesting projects.

I want to thank all my colleagues and former members of our group. Tuomas, you have taught me so many practical things. I learned almost all the chemistry and biology related-work from you, and you were the mentor in the area. We worked so much together on osteoclasts as my wife almost got jealous at you. I really enjoyed working with you. Sami, you were my teacher for many things and, having similar background, I enjoyed sharing thoughts and discussing new science with you. Later on, as friends, together with our wives, we really enjoyed inviting and being invited for dinners. Also traveling with you, such a gourmet, was awesome. Elnaz, thank you for your supports in the OC project. You have been a steady learner and it was fun seeing big improvements in you. I look forward to your success in science. Kai-lan, thank you for your hard work on the fly project taking many weekends. You were a quick learner and had really skillful hands. I wish you all the best after your coming degree. Neeraj and Janne, you were the Bad Boys, bringing new atmosphere and “enthusiasm” to the group. I enjoyed joking with you during your coffee time. Eija and Anita, thank you for helping me in the wet lab and in, personal, baby-related matters. Elena, I enjoyed working with you with mice and flies, and Markus, thank you for teaching me EM. I also would like to acknowledge all the former members, Kari V., Qi, Laura, Mikko, Karthik, Madis, Harri, Sari, Kari K., Roope H..

Thanks to all the imaging-related people, especially Jouko and Markku in CIC for your generous technical supports, and Pasi, Jari, Petra, Inga, Joanna, Eeva, and Maritta in Turku Bioimaging. I want to thank Vesa for technical supports with Leica microscopes, and Aura Professional English Consulting, Ltd. for providing the linguistic editing of this manuscript. I also thank all the nice people in Biocity, especially Maja, Camilo, Tomoko, for nice chats.

All my Japanese friends, especially Dr. Sakurai, Prof. Endo, Dr. Fujii, Prof. Miyasaka, as well as other Japanese friends in Turku are acknowledged. I enjoyed sharing life experiences and feelings about

Finland with you. Madame Yasuko is acknowledged for supports during start-up in Finland. All the nice people from my Nokia-related work are acknowledged. It brought me all the way to Finland and I found it was a right choice.

Gratitude goes to my parents, Kazuo and Mikiko Deguchi for raising me and giving me a chance for good education. Also many thanks to my siblings, Michihito, Yoko, and Ryosuke. Another gratitude goes to my grandmother, Fumi, who wished to visit to see the defense. I want to thank my very close friends, Enomoto-sensei, and Dr. Itokazu for tremendous amount of encouragements during my study. I thank all my friends of Buddhism practitioners, especially Elvi, Ritva-Liisa, Maiju, Jarmo, Timo, Emma, Benedikt, and Ivo, for their friendships and encouragements. With my deepest respect, I wish to sincerely thank Dr. Daisaku Ikeda for the guidance in my life.

And the greatest gratitude and respect goes to my dearest wife, Michiko. You have believed in me and encouraged me with millions of smiles and your inherent optimism. Your trust on me brought my research this far. Thank you for your patience on living abroad away from families, working in an unfamiliar job, caring for my health, and being a wonderful cook. Living with you, my life has become so colorful. Furthermore, I would like to thank you for the lovely gift, our daughter Kokoro. Our life has become astonishing and magical after the birth.

November 18th, 2015 Turku, Finland

8 REFERENCES

Abbe, E. (1873). Beiträge zur Theorie des Mikroskops und der mikroskopischen Wahrnehmung. Arch. Für Mikrosk. Anat. *9*, 413–418.

Akisaka, T., and Yoshida, A. (2015). Visualization of structural organization of ventral membranes of sheared-open resorbing osteoclasts attached to apatite pellets. Cell Tissue Res. *360*, 347–362.

Akisaka, T., Yoshida, H., and Suzuki, R. (2006). The ruffled border and attachment regions of the apposing membrane of resorbing osteoclasts as visualized from the cytoplasmic face of the membrane. J. Electron Microsc. (Tokyo) *55*, 53–61.

Bailey, B., Farkas, D.L., Taylor, D.L., and Lanni, F. (1993). Enhancement of axial resolution in fluorescence microscopy by standing-wave excitation. Nature *366*, 44–48.

Bates, M., Huang, B., Dempsey, G.T., and Zhuang, X. (2007). Multicolor Super-Resolution Imaging with Photo-Switchable Fluorescent Probes. Science *317*, 1749–1753.

Berglund, A.J., McMahon, M.D., McClelland, J.J., and Liddle, J.A. (2009). Imaging Response of Optical Microscopes Containing Angled Micromirrors. In Advances in Imaging, (Optical Society of America), p. NWB5.

Berglund, A.J., McMahon, M.D., McClelland, J.J., and Liddle, J.A. (2010). Theoretical model of errors in micromirror-based three-dimensional particle tracking. Opt. Lett. *35*, 1905–1907.

Berning, S., Willig, K.I., Steffens, H., Dibaj, P., and Hell, S.W. (2012). Nanoscopy in a Living Mouse Brain. Science *335*, 551–551.

Bethge, P., Chéreau, R., Avignone, E., Marsicano, G., and Nägerl, U.V. (2013). Two-Photon Excitation STED Microscopy in Two Colors in Acute Brain Slices. Biophys. J. *104*, 778–785.

Betzig, E. (1995). Proposed method for molecular optical imaging. Opt. Lett. *20*, 237.

Betzig, E., Patterson, G.H., Sougrat, R., Lindwasser, O.W., Olenych,

S., Bonifacino, J.S., Davidson, M.W., Lippincott-Schwartz, J., and Hess, H.F. (2006). Imaging Intracellular Fluorescent Proteins at Nanometer Resolution. Science *313*, 1642–1645.

Blanca, C., and Hell, S. (2002). Axial superresolution with ultrahigh aperture lenses. Opt. Express *10*, 893.

Bradl, J., Hausmann, M., Ehemann, V., Komitowski, D., and Cremer, C. (1992). A tilting device for three-dimensional microscopy: Application to in situ imaging of interphase cell nuclei. J. Microsc. *168*, 47–57.

Bradl, J., Hausmann, M., Schneider, B., Rinke, B., and Cremer, C. (1994). A versatile 2π-tilting device for fluorescence microscopes. J. Microsc. *176*, 211–221.

Bradl, J., Rinke, B., Edelmann, S., Edelmann, P., Krieger, H., Hausmann, M., and Cremer, C. (1996). Resolution improvement in 3D fluorescence microscopy by object tilting. Microsc. Anal.

Bretschneider, S., Eggeling, C., and Hell, S.W. (2007). Breaking the Diffraction Barrier in Fluorescence Microscopy by Optical Shelving. Phys. Rev. Lett. *98*, 218103.

Brinkmann, J., Hefti, T., Schlottig, F., Spencer, N.D., and Hall, H. (2012). Response of Osteoclasts to Titanium Surfaces with Increasing Surface Roughness: An In Vitro Study. Biointerphases *7*, 1–9.

Bruzzaniti, A., Neff, L., Sanjay, A., Horne, W.C., De Camilli, P., and Baron, R. (2005). Dynamin Forms a Src Kinase–sensitive Complex with Cbl and Regulates Podosomes and Osteoclast Activity. Mol. Biol. Cell *16*, 3301–3313.

Cameron, L.A., Svitkina, T.M., Vignjevic, D., Theriot, J.A., and Borisy, G.G. (2001). Dendritic organization of actin comet tails. Curr. Biol. *11*, 130–135.

Chambers, T.J., Revell, P.A., Fuller, K., and Athanasou, N.A. (1984). Resorption of bone by isolated rabbit osteoclasts. J. Cell Sci. *66*, 383–399.

Chmyrov, A., Keller, J., Grotjohann, T., Ratz, M., d'Este, E., Jakobs,

S., Eggeling, C., and Hell, S.W. (2013). Nanoscopy with more than 100,000 “doughnuts.” Nat. Methods *10*, 737–740.

Cogswell, C.J., Larkin, K.G., and Klemm, H.U. (1996). Fluorescence microtomography: multiangle image acquisition and 3D digital reconstruction. In Proceedings of SPIE, pp. 109–115.

Collins, A., Warrington, A., Taylor, K.A., and Svitkina, T. (2011). Structural Organization of the Actin Cytoskeleton at Sites of Clathrin-Mediated Endocytosis. Curr. Biol. *21*, 1167–1175.

Corle, T., and Kino, G. (1996). Confocal Scanning Optical Microscopy and Related Imaging Systems (Burlington: Academic Press).

Cox, S., Rosten, E., Monypenny, J., Jovanovic-Talisman, T., Burnette, D.T., Lippincott-Schwartz, J., Jones, G.E., and Heintzmann, R. (2012). Bayesian localization microscopy reveals nanoscale podosome dynamics. Nat. Methods *9*, 195–200.

Deschout, H., Zanacchi, F.C., Mlodzianoski, M., Diaspro, A., Bewersdorf, J., Hess, S.T., and Braeckmans, K. (2014). Precisely and accurately localizing single emitters in fluorescence microscopy. Nat. Methods *11*, 253–266.

Destaing, O., Saltel, F., Géminard, J.-C., Jurdic, P., and Bard, F. (2003). Podosomes Display Actin Turnover and Dynamic Self-Organization in Osteoclasts Expressing Actin-Green Fluorescent Protein. Mol. Biol. Cell *14*, 407–416.

Dickson, R.M., Cubitt, A.B., Tsien, R.Y., and Moerner, W.E. (1997). On/off blinking and switching behaviour of single molecules of green fluorescent protein. Nature *388*, 355–358.

Dominguez, R., and Holmes, K.C. (2011). Actin Structure and Function. Annu. Rev. Biophys. *40*, 169–186.

van den Dries, K., Meddens, M.B.M., de Keijzer, S., Shekhar, S., Subramaniam, V., Figdor, C.G., and Cambi, A. (2013). Interplay between myosin IIA-mediated contractility and actin network integrity orchestrates podosome composition and oscillations. Nat. Commun. *4*, 1412.

van den Dries, K., Bolomini-Vittori, M., and Cambi, A. (2014). Spatiotemporal organization and mechanosensory function of podosomes. Cell Adhes. Migr. *8*, 268–272.

Duong, L.T., and Rodan, G.A. (1999). The role of integrins in osteoclast function. J. Bone Miner. Metab. *17*, 1–6.

Dyba, M., and Hell, S.W. (2002). Focal Spots of Size λ/23 Open Up Far-Field Florescence Microscopy at 33 nm Axial Resolution. Phys. Rev. Lett. *88*, 163901.

Endesfelder, U., and Heilemann, M. (2014). Art and artifacts in single-molecule localization microscopy: beyond attractive images. Nat. Methods *11*, 235–238.

Engelhardt, J., Keller, J., Hoyer, P., Reuss, M., Staudt, T., and Hell, S.W. (2011). Molecular Orientation Affects Localization Accuracy in Superresolution Far-Field Fluorescence Microscopy. Nano Lett. *11*, 209–213.

Fölling, J., Bossi, M., Bock, H., Medda, R., Wurm, C.A., Hein, B., Jakobs, S., Eggeling, C., and Hell, S.W. (2008). Fluorescence nanoscopy by ground-state depletion and single-molecule return. Nat. Methods *5*, 943–945.

Francia, G.T.D. (1952). Super-gain antennas and optical resolving power. Il Nuovo Cimento *9*, 426–438.

Fuller, K., Ross, J.L., Szewczyk, K.A., Moss, R., and Chambers, T.J. (2010). Bone Is Not Essential for Osteoclast Activation. PLoS ONE *5*, e12837.

Gawden-Bone, C., Zhou, Z., King, E., Prescott, A., Watts, C., and Lucocq, J. (2010). Dendritic cell podosomes are protrusive and invade the extracellular matrix using metalloproteinase MMP-14. J. Cell Sci. *123*, 1427–1437.

Geblinger, D., Addadi, L., and Geiger, B. (2010). Nano-Topography Sensing by Osteoclasts. J. Cell Sci. *123*, 1503–1510.

Giannone, G., Hosy, E., Levet, F., Constals, A., Schulze, K., Sobolevsky, A.I., Rosconi, M.P., Gouaux, E., Tampé, R., Choquet, D.,

et al. (2010). Dynamic Superresolution Imaging of Endogenous Proteins on Living Cells at Ultra-High Density. Biophys. J. *99*, 1303–1310.

Gould, T.J., Burke, D., Bewersdorf, J., and Booth, M.J. (2012). Adaptive optics enables 3D STED microscopy in aberrating specimens. Opt. Express *20*, 20998–21009.

Gustafsson, M.G.L. (2000). Surpassing the lateral resolution limit by a factor of two using structured illumination microscopy. J. Microsc. *198*, 82–87.

Gustafsson, M.G.L. (2005). Nonlinear structured-illumination microscopy: Wide-field fluorescence imaging with theoretically unlimited resolution. Proc. Natl. Acad. Sci. U. S. A. *102*, 13081–13086.

Gustafsson, Agard, and Sedat (1999). I5M: 3D widefield light microscopy with better than 100 nm axial resolution. J. Microsc. *195*, 10–16.

Gustafsson, M.G.L., Agard, D.A., and Sedat, J.W. (1995). Sevenfold improvement of axial resolution in 3D wide-field microscopy using two objective lenses. In Proceedings of SPIE, pp. 147–156.

Gustafsson, M.G.L., Shao, L., Carlton, P.M., Wang, C.J.R., Golubovskaya, I.N., Cande, W.Z., Agard, D.A., and Sedat, J.W. (2008). Three-Dimensional Resolution Doubling in Wide-Field Fluorescence Microscopy by Structured Illumination. Biophys. J. *94*, 4957–4970.

Hajjoul, H., Kocanova, S., Lassadi, I., Bystricky, K., and Bancaud, A. (2009). Lab-on-Chip for fast 3D particle tracking in living cells. Lab. Chip *9*, 3054.

Hänninen, P.E., Hell, S.W., Salo, J., Soini, E., and Cremer, C. (1995). Two-photon excitation 4Pi confocal microscope: Enhanced axial resolution microscope for biological research. Appl. Phys. Lett. *66*, 1698–1700.

Harke, B., Ullal, C.K., Keller, J., and Hell, S.W. (2008). Three-Dimensional Nanoscopy of Colloidal Crystals. Nano Lett. *8*, 1309–1313.

Heervä, E., Alanne, M.H., Peltonen, S., Kuorilehto, T., Hentunen, T., Väänänen, K., and Peltonen, J. (2010). Osteoclasts in neurofibromatosis type 1 display enhanced resorption capacity, aberrant morphology, and resistance to serum deprivation. Bone *47*, 583–590.

Heilemann, M., van de Linde, S., Schüttpelz, M., Kasper, R., Seefeldt, B., Mukherjee, A., Tinnefeld, P., and Sauer, M. (2008). Subdiffraction-Resolution Fluorescence Imaging with Conventional Fluorescent Probes. Angew. Chem. Int. Ed. *47*, 6172–6176.

Heintzmann, R., and Cremer, C. (2002). Axial tomographic confocal fluorescence microscopy. J. Microsc. *206*, 7–23.

Heintzmann, R., and Cremer, C.G. (1999). Laterally modulated excitation microscopy: improvement of resolution by using a diffraction grating. In Proceedings of SPIE, pp. 185–196.

Hell, S.W. (2003). Toward fluorescence nanoscopy. Nat Biotech *21*, 1347–1355.

Hell, S.W. (2004). Strategy for far-field optical imaging and writing without diffraction limit. Phys. Lett. A *326*, 140–145.

Hell, S.W. (2009). Microscopy and its focal switch. Nat Meth *6*, 24–32.

Hell, S., and Stelzer, E.H.K. (1992). Properties of a 4Pi confocal fluorescence microscope. J. Opt. Soc. Am. A *9*, 2159–2166.

Hell, S.W., and Kroug, M. (1995). Ground-state-depletion fluorscence microscopy: A concept for breaking the diffraction resolution limit. Appl. Phys. B *60*, 495–497.

Hell, S.W., and Wichmann, J. (1994). Breaking the diffraction resolution limit by stimulated emission: stimulated-emission-depletion fluorescence microscopy. Opt. Lett. *19*, 780–782.

Hell, S.W., Schrader, M., Bahlmann, K., Meinecke, F., Lakowicz, J.R., and Gryczynski, I. (1995). Stimulated emission on microscopic scale: Light quenching of Pyridine 2 using a Ti:sapphire laser. J. Microsc. *180*, RP1–RP2.

Hirvonen, M.J., Fagerlund, K., Lakkakorpi, P., Väänänen, H.K., and Mulari, M.T.K. (2013). Novel perspectives on the transcytotic route in osteoclasts. BoneKEy Rep. *2*.

Hofmann, M., Eggeling, C., Jakobs, S., and Hell, S.W. (2005). Breaking the diffraction barrier in fluorescence microscopy at low light intensities by using reversibly photoswitchable proteins. Proc. Natl. Acad. Sci. U. S. A. *102*, 17565–17569.

Huang, B., Wang, W., Bates, M., and Zhuang, X. (2008). Three-Dimensional Super-Resolution Imaging by Stochastic Optical Reconstruction Microscopy. Science *319*, 810–813.

Irene Rita, and Maragos Hurst (2006). Study of the Actin-Related Protein 2/3 complex and osteoclast bone resorption. University of Florida.

Kaksonen, M., Toret, C.P., and Drubin, D.G. (2006). Harnessing actin dynamics for clathrin-mediated endocytosis. Nat. Rev. Mol. Cell Biol. *7*, 404–414.

Kanchanawong, P., Shtengel, G., Pasapera, A.M., Ramko, E.B., Davidson, M.W., Hess, H.F., and Waterman, C.M. (2010). Nanoscale architecture of integrin-based cell adhesions. Nature *468*, 580–584.

Klar, T.A., and Hell, S.W. (1999). Subdiffraction resolution in far-field fluorescence microscopy. Opt. Lett. *24*, 954.

Klar, T.A., Jakobs, S., Dyba, M., Egner, A., and Hell, S.W. (2000). Fluorescence microscopy with diffraction resolution barrier broken by stimulated emission. Proc. Natl. Acad. Sci. *97*, 8206–8210.

Koho, S., Deguchi, T., and Hänninen, P.E. (2015). A software tool for tomographic axial superresolution in STED microscopy. J. Microsc. n/a – n/a.

Lakkakorpi, P., Tuukkanen, J., Hentunen, T., Järvelin, K., and Väänänen, K. (1989). Organization of osteoclast microfilaments during the attachment to bone surface in vitro. J. Bone Miner. Res. *4*, 817–825.

Laksameethanasan, D., Brandt, S.S., and Engelhardt, P. (2006). A

three-dimensional Bayesian reconstruction method with the point spread function for micro-rotation sequences in wide-field microscopy. In 3rd IEEE International Symposium on Biomedical Imaging: Nano to Macro, 2006, pp. 1276–1279.

Lee, H.D., Sahl, S.J., Lew, M.D., and Moerner, W.E. (2012). The double-helix microscope super-resolves extended biological structures by localizing single blinking molecules in three dimensions with nanoscale precision. Appl. Phys. Lett. *100*, 153701–153701 – 3.

van de Linde, S., Löschberger, A., Klein, T., Heidbreder, M., Wolter, S., Heilemann, M., and Sauer, M. (2011). Direct stochastic optical reconstruction microscopy with standard fluorescent probes. Nat. Protoc. *6*, 991–1009.

Lizundia, R., Sengmanivong, L., Guergnon, J., Müller, T., Schnelle, T., Langsley, G., and Shorte, S.L. (2005). Use of micro-rotation imaging to study JNK-mediated cell survival in Theileria parva-infected B-lymphocytes. Parasitology *130*, 629–635.

Luxenburg, C., Geblinger, D., Klein, E., Anderson, K., Hanein, D., Geiger, B., and Addadi, L. (2007). The Architecture of the Adhesive Apparatus of Cultured Osteoclasts: From Podosome Formation to Sealing Zone Assembly. PLoS ONE *2*, e179.

Luxenburg, C., Winograd-Katz, S., Addadi, L., and Geiger, B. (2012). Involvement of actin polymerization in podosome dynamics. J. Cell Sci. *125*, 1666–1672.

Marchisio, P.C., Cirillo, D., Naldini, L., Primavera, M.V., Teti, A., and Zambonin-Zallone, A. (1984). Cell-substratum interaction of cultured avian osteoclasts is mediated by specific adhesion structures. J. Cell Biol. *99*, 1696–1705.

Mark, A.E., Davis, M.A., Starosta, M.S., and Dunn, A.K. (2015). Computational modeling of STED microscopy through multiple biological cells under one- and two-photon excitation. In Proceedings of SPIE, p. 93300V.

McMahon, M.D., Berglund, A.J., Carmichael, P., McClelland, J.J., and Liddle, J.A. (2009). 3D Particle Trajectories Observed by Orthogonal Tracking Microscopy. ACS Nano *3*, 609–614.

McMichael, B.K., Cheney, R.E., and Lee, B.S. (2010). Myosin X Regulates Sealing Zone Patterning in Osteoclasts through Linkage of Podosomes and Microtubules. J. Biol. Chem. *285*, 9506–9515.

Mettlen, M., Pucadyil, T., Ramachandran, R., and Schmid, S.L. (2009). Dissecting dynamin's role in clathrin-mediated endocytosis. Biochem. Soc. Trans. *37*, 1022–1026.

Micheva, K.D., and Smith, S.J. (2007). Array Tomography: A New Tool for Imaging the Molecular Architecture and Ultrastructure of Neural Circuits. Neuron *55*, 25–36.

Mooren, O.L., Galletta, B.J., and Cooper, J.A. (2012). Roles for Actin Assembly in Endocytosis. Annu. Rev. Biochem. *81*, 661–686.

Mulari, M.T.K., Zhao, H., Lakkakorpi, P.T., and Väänänen, H.K. (2003). Osteoclast Ruffled Border Has Distinct Subdomains for Secretion and Degraded Matrix Uptake. Traffic *4*, 113–125.

Nägerl, U.V., Willig, K.I., Hein, B., Hell, S.W., and Bonhoeffer, T. (2008). Live-cell imaging of dendritic spines by STED microscopy. Proc. Natl. Acad. Sci. *105*, 18982–18987.

Nanguneri, S., Flottmann, B., Horstmann, H., Heilemann, M., and Kuner, T. (2012). Three-Dimensional, Tomographic Super-Resolution Fluorescence Imaging of Serially Sectioned Thick Samples. PLoS ONE *7*, e38098.

Nesbitt, S.A., and Horton, M.A. (1997). Trafficking of Matrix Collagens Through Bone-Resorbing Osteoclasts. Science *276*, 266–269.

Novack, D.V., and Faccio, R. (2011). Osteoclast motility: Putting the brakes on bone resorption. Ageing Res. Rev. *10*, 54–61.

Olivier, N., Keller, D., Rajan, V.S., Gönczy, P., and Manley, S. (2013). Simple buffers for 3D STORM microscopy. Biomed. Opt. Express *4*, 885.

Palokangas, H., Mulari, M., and Väänänen, H.K. (1997). Endocytic pathway from the basal plasma membrane to the ruffled border membrane in bone-resorbing osteoclasts. J. Cell Sci. *110 (Pt 15)*,

1767–1780.

Patterson, G.H., and Lippincott-Schwartz, J. (2002). A photoactivatable GFP for selective photolabeling of proteins and cells. Science *297*, 1873–1877.

Pfaff, M., and Jurdic, P. (2001). Podosomes in osteoclast-like cells structural analysis and cooperative roles of paxillin, proline-rich tyrosine kinase 2 (Pyk2) and integrin αVβ3. J. Cell Sci. *114*, 2775–2786.

Praefcke, G.J.K., and McMahon, H.T. (2004). The dynamin superfamily: universal membrane tubulation and fission molecules? Nat. Rev. Mol. Cell Biol. *5*, 133–147.

Rayleigh, Lord (1903). On the Theory of Optical Images, with special reference to the Microscope. J. R. Microsc. Soc. *23*, 474–482.

Redey, S.A., Razzouk, S., Rey, C., Bernache-Assollant, D., Leroy, G., Nardin, M., and Cournot, G. (1999). Osteoclast adhesion and activity on synthetic hydroxyapatite, carbonated hydroxyapatite, and natural calcium carbonate: Relationship to surface energies. J. Biomed. Mater. Res. *45*, 140–147.

Remmele, S., Oehm, B., Staier, F., Eipel, H., Cremer, C., and Hesser, J. (2011). Reconstruction of high-resolution fluorescence microscopy images based on axial tomography. In Proceedings of SPIE, p. 79624O.

Rubio-Guivernau, J.L., Gurchenkov, V., Luengo-Oroz, M.A., Duloquin, L., Bourgine, P., Santos, A., Peyrieras, N., and Ledesma-Carbayo, M.J. (2012). Wavelet-based image fusion in multi-view three-dimensional microscopy. Bioinformatics *28*, 238–245.

Rust, M.B., and Maritzen, T. (2015). Relevance of presynaptic actin dynamics for synapse function and mouse behavior. Exp. Cell Res. *335*, 165–171.

Rust, M.J., Bates, M., and Zhuang, X. (2006). Sub-diffraction-limit imaging by stochastic optical reconstruction microscopy (STORM). Nat. Methods *3*, 793–796.

Salo, J., Lehenkari, P., Mulari, M., Metsikkö, K., and Väänänen, H.K. (1997). Removal of Osteoclast Bone Resorption Products by Transcytosis. Science *276*, 270–273.

Saltel, F., Destaing, O., Bard, F., Eichert, D., and Jurdic, P. (2004). Apatite-Mediated Actin Dynamics in Resorbing Osteoclasts. Mol. Biol. Cell *15*, 5231–5241.

Sätzler, K., and Eils, R. (1997). Resolution improvement by 3-D reconstructions from tilted views in axial tomography and confocal theta microscopy. Bioimaging *5*, 171–182.

Saux, B.L., Chalmond, B., Yu, Y., Trouvé, A., Renaud, O., and Shorte, S. l. (2009). Isotropic high-resolution three-dimensional confocal micro-rotation imaging for non-adherent living cells. J. Microsc. *233*, 404–416.

Schermelleh, L., Heintzmann, R., and Leonhardt, H. (2010). A guide to super-resolution fluorescence microscopy. J. Cell Biol. *190*, 165–175.

Schmidt, R., Wurm, C.A., Jakobs, S., Engelhardt, J., Egner, A., and Hell, S.W. (2008). Spherical nanosized focal spot unravels the interior of cells. Nat. Methods *5*, 539–544.

Schmidt, R., Wurm, C., Punge, A., Egner, A., Jakobs, S., and Hell, S. (2009). Mitochondrial cristae revealed with focused light. Nano Lett *9*, 2508–2510.

Schneider, J., Zahn, J., Maglione, M., Sigrist, S.J., Marquard, J., Chojnacki, J., Kräusslich, H.-G., Sahl, S.J., Engelhardt, J., and Hell, S.W. (2015). Ultrafast, temporally stochastic STED nanoscopy of millisecond dynamics. Nat. Methods *advance online publication*.

Seale, K. t., Reiserer, R. s., Markov, D. a., Ges, I. a., Wright, C., Janetopoulos, C., and Wikswo, J. p. (2008). Mirrored pyramidal wells for simultaneous multiple vantage point microscopy. J. Microsc. *232*, 1–6.

Sharonov, A., and Hochstrasser, R.M. (2006). Wide-field subdiffraction imaging by accumulated binding of diffusing probes. Proc. Natl. Acad. Sci. *103*, 18911–18916.

Shaw, P.J., Agard, D.A., Hiraoka, Y., and Sedat, J.W. (1989). Tilted view reconstruction in optical microscopy. Three-dimensional reconstruction of Drosophila melanogaster embryo nuclei. Biophys. J. *55*, 101–110.

Sheppard, C.J.R. (1977). The use of lenses with annular aperture in scanning optical microscopy. Optik.

Sheppard, C.J.R., and Choudhury, A. (2004). Annular Pupils, Radial Polarization, and Superresolution. Appl. Opt. *43*, 4322–4327.

Shibutani, T., Iwanaga, H., Imai, K., Kitago, M., Doi, Y., and Iwayama, Y. (2000). Use of glass slides coated with apatite–collagen complexes for measurement of osteoclastic resorption activity. J. Biomed. Mater. Res. *50*, 153–159.

Shroff, S.A., Fienup, J.R., and Williams, D.R. (2008). OTF compensation in structured illumination superresolution images. In Proceedings of SPIE, p. 709402.

Shtengel, G., Galbraith, J.A., Galbraith, C.G., Lippincott-Schwartz, J., Gillette, J.M., Manley, S., Sougrat, R., Waterman, C.M., Kanchanawong, P., Davidson, M.W., et al. (2009). Interferometric fluorescent super-resolution microscopy resolves 3D cellular ultrastructure. Proc. Natl. Acad. Sci. *106*, 3125–3130.

Skaer, R.J., and Whytock, S. (1975). Interpretation of the three-dimensional structure of living nuclei by specimen tilt. J. Cell Sci. *19*, 1–10.

Small, J.V., Stradal, T., Vignal, E., and Rottner, K. (2002). The lamellipodium: where motility begins. Trends Cell Biol. *12*, 112–120.

Smythe, E., and Ayscough, K.R. (2006). Actin regulation in endocytosis. J. Cell Sci. *119*, 4589–4598.

Staudt, T., Lang, M.C., Medda, R., Engelhardt, J., and Hell, S.W. (2007). 2,2′-Thiodiethanol: A new water soluble mounting medium for high resolution optical microscopy. Microsc. Res. Tech. *70*, 1–9.

Stenbeck, G. (2002). Formation and function of the ruffled border in osteoclasts. Semin. Cell Dev. Biol. *13*, 285–292.

Stenbeck, G., and Horton, M.A. (2004). Endocytic trafficking in actively resorbing osteoclasts. J. Cell Sci. *117*, 827–836.

Svitkina, T.M. (2013). Ultrastructure of protrusive actin filament arrays. Curr. Opin. Cell Biol. *25*, 574–581.

Szewczyk, K.A., Fuller, K., and Chambers, T.J. (2013). Distinctive Subdomains in the Resorbing Surface of Osteoclasts. PLoS ONE *8*, e60285.

Takahashi, N., Udagawa, N., and Suda, T. (2014). Vitamin D endocrine system and osteoclasts. BoneKEy Rep. *3*.

Tang, J., Akerboom, J., Vaziri, A., Looger, L.L., and Shank, C.V. (2010). Near-isotropic 3D optical nanoscopy with photon-limited chromophores. Proc. Natl. Acad. Sci. *107*, 10068–10073.

Teitelbaum, S.L. (2000). Bone Resorption by Osteoclasts. Science *289*, 1504–1508.

Theriot, J.A. (2000). The Polymerization Motor. Traffic *1*, 19–28.

Thompson, R.E., Larson, D.R., and Webb, W.W. (2002). Precise Nanometer Localization Analysis for Individual Fluorescent Probes. Biophys. J. *82*, 2775–2783.

Urban, N.T., Willig, K.I., Hell, S.W., and Nägerl, U.V. (2011). STED Nanoscopy of Actin Dynamics in Synapses Deep Inside Living Brain Slices. Biophys. J. *101*, 1277–1284.

Väänänen, H.K., and Horton, M. (1995). The osteoclast clear zone is a specialized cell-extracellular matrix adhesion structure. J. Cell Sci. *108*, 2729–2732.

Vicente-Manzanares, M., Ma, X., Adelstein, R.S., and Horwitz, A.R. (2009). Non-muscle myosin II takes centre stage in cell adhesion and migration. Nat. Rev. Mol. Cell Biol. *10*, 778–790.

Vicidomini, G., Moneron, G., Han, K.Y., Westphal, V., Ta, H., Reuss, M., Engelhardt, J., Eggeling, C., and Hell, S.W. (2011). Sharper low-power STED nanoscopy by time gating. Nat. Methods *8*, 571–573.

Vicidomini, G., Coto Hernández, I., d'Amora, M., Cella Zanacchi, F.,

Bianchini, P., and Diaspro, A. (2014). Gated CW-STED microscopy: A versatile tool for biological nanometer scale investigation. Methods *66*, 124–130.

Walde, M., Monypenny, J., Heintzmann, R., Jones, G.E., and Cox, S. (2014). Vinculin Binding Angle in Podosomes Revealed by High Resolution Microscopy. PLoS ONE *9*, e88251.

Wildanger, D., Patton, B.R., Schill, H., Marseglia, L., Hadden, J.P., Knauer, S., Schönle, A., Rarity, J.G., O'Brien, J.L., Hell, S.W., et al. (2012). Solid Immersion Facilitates Fluorescence Microscopy with Nanometer Resolution and Sub-Ångström Emitter Localization. Adv. Mater. Deerfield Beach Fla *24*, OP309–OP313.

Willig, K.I., Keller, J., Bossi, M., and Hell, S.W. (2006). STED microscopy resolves nanoparticle assemblies. New J. Phys. *8*, 106.

York, A.G., Parekh, S.H., Nogare, D.D., Fischer, R.S., Temprine, K., Mione, M., Chitnis, A.B., Combs, C.A., and Shroff, H. (2012). Resolution doubling in live, multicellular organisms via multifocal structured illumination microscopy. Nat. Methods *9*, 749–754.